# Highlights

Parallel simulation and adaptive mesh refinement for 3D elastostatic contact mechanics problems between deformable bodies

EPALLE Alexandre<sup>1,2</sup>, RAMIÈRE Isabelle<sup>1</sup>, LATU Guillaume<sup>1</sup>, LEBON Frédéric<sup>2</sup>

- Combinaison of adaptive mesh refinement and contact in a parallel finite element framework
- Non-conforming h-adaptive refinement on quadrilateral and hexahedral meshes
- Super-parametric elements to deal with curved geometries during the AMR process
- Mesh partitioning ensuring contact paired nodes on the same MPI tasks
- Very satisfactory strong scalability up to 1024 cores.

# Parallel simulation and adaptive mesh refinement for 3D elastostatic contact mechanics problems between deformable bodies

EPALLE Alexandre<sup>1,2</sup>, RAMIÈRE Isabelle<sup>1</sup>, LATU Guillaume<sup>1</sup>, LEBON Frédéric<sup>2</sup>

- <sup>1</sup> CEA, DES, IRESNE, DEC, SESC; Cadarache, F-13108 Saint-Paul-Lez Durance, France
- <sup>2</sup> Aix-Marseille Université, CNRS, Centrale Marseille, LMA ; F-13453 Marseille cedex 13, France

This preprint corresponds to the Chapter 7 of volume 61 in AAMS, Advances in Applied Mechanics.

#### Abstract

Parallel implementation of numerical adaptive mesh refinement (AMR) strategies for solving 3D elastostatic contact mechanics problems is an essential step toward complex simulations that exceed current performance levels. This paper introduces a scalable, robust, and efficient algorithm to deal with 2D and 3D elastostatics contact problems between deformable bodies in a finite element framework. The proposed solution combines a treatment of the contact problem by a node-to-node pairing algorithm with a penalization technique and a non-conforming h-adaptive refinement of quadrilateral/hexahedral meshes based on an estimate-mark-refine approach in a parallel framework. One of the special features of our parallel strategy is that contact paired nodes are hosted by the same MPI tasks, which reduces the number of exchanges between processes for building the contact operator. The mesh partitioning introduced in this paper respects this rule and is based on an equidistribution of elements over processes, without any other constraints. In order to preserve the domain curvature while hierarchical mesh refinement, super-parametric elements are used. This functionality enables the contact zone to be well detected during the AMR process, even for an initial coarse mesh and low-order discretization schemes. The efficiency of our contact-AMR-HPC strategy is assessed on 2D and 3D Hertzian contact problems. Different AMR detection criteria are considered. Various convergence analyses are conducted. Parallel performances up to 1024 cores are illustrated. Furthermore, memory footprint and preconditionners performance are analyzed.

Keywords: Contact mechanics problems, Adaptive mesh refinement, High performance computing, Elastostaticity, Node-to-node pairing, Element equidistribution partitioning

#### 1. Introduction

Efficient numerical solving of contact mechanics problems remains challenging. These problems are locally highly non-linear and non-smooth. They often have the particularity of concentrating very high stress in the contact area. Thus, the numerical simulation of this type of problems is computationally demanding, especially if a local accurate solution is expected.

Dealing with contact between deformable solids, the finite element method (FEM) [1] remains the most widely used numerical method [2] for solving the associated problem, although others approaches have been more recently introduced. Let us cite for example the virtual element method (VEM) [3, 4] and its extension to contact [5, 6] as well as the Hybrid High Order (HHO) [7, 8] and its adaptation to (frictional) contact problems [9]. The scaled boundary finite element method (SBFEM) [10], combining the advantages of the FEM and of the boundary element method (BEM), has also been recently applied for contact analysis in [11]. Finally, let us mention the work on isogeometric contact [12] which considers contact formulations within the framework of isogeometric analysis (IGA) [13].

Several numerical strategies have been developed over the years to deal with constraints at contact interfaces [14, 15, 2]. When using the FEM, the penalization method [16], the Lagrange multiplier method [14], the augmented Lagrangian method [17], the Nitsche method [18, 19] or mortar-based formulation [20] are commonly employed to design robust and efficient algorithms. For more details about these strategies, the reader is referred to [2].

Furthermore, solving contact problems with accuracy requires a high degree of mesh refinement in the contact zones. Building uniformly refined mesh for such problems is still prohibitively computationally expensive, especially for 3D geometries. One way to overcome this limit is to rely on adaptive mesh refinement (AMR) methods [21]. These techniques, which have been well known for many years, enable the mesh to be locally adjusted to a de-

sired accuracy, thereby reducing the total number of degrees of freedom compared to uniformly refined meshes. Popular adaptive techniques for reducing discretization error include h-adaptive [22, 23] (mesh-step refinement), p-adaptive [24, 25] (order of basis function increase), hp-adaptive [26, 25] (combination of both previous) and local multigrid [27, 28, 29] approaches (geometric refinement by adding local refined meshes). Adaptive mesh refinement is generally coupled with a posteriori error estimators [21] in order to automatically determine the elements to be refined, and sometimes also to automatically stop the refinement process [30, 31].

Many works have focused on the application of AMR techniques in the context of contact mechanics problems, mainly in the FEM framework. Let us cite for example [32, 33, 34, 35] whose authors proposed dedicated a posteriori error estimators for contact problems that have been applied with conforming h-adaptive refinement. In particular, [32] modifies the Zienkiewicz and Zhu (ZZ) estimator [30] to take into account contact contributions. In their turn, the works of [36, 37] focus on mesh adaptivity with non-conforming hrefinement methods. Adaptation of local multigrid methods for contact problems have been studied in [38, 31]. Let us mention that the authors of [31] successfully applied the standard ZZ estimator in each body separately as for multimaterial problems. Most of the above methods have only been applied on 2D geometries. It should also be noted that some of them only concern rigid-deformable contact problems (Signorini problems) [33, 36, 37, 35]. For its part, the extension of SBFEM to contact problems [11] has been directly introduced in a non-conforming h-adaptive mesh framework based on a quadtree decomposition with a dedicated SBFEM error indicator [39]. Concerning the VEM, the authors in [40] provide a methodology to combine AMR and 2D contact problems. Two types of AMR techniques are studied on 2D contact problems: non-conforming h-adaptive meshes or conforming locally refined Voronoï cell meshes. The mesh is locally refined in a predefined contact zone until a geometric criterion on the refined contact area is reached. The extension to 3D contact problems of the VEM with AMR based on Voronoï type elements is proposed in [41].

However, for highly singular problems such as those arising from contact mechanics, the discretization can become very fine locally, and the number of unknowns prohibitive even with AMR. It is therefore also desirable to use high-performance computing (HPC) methods for faster processing and for handling large-scale problems. The fast solution of partial differential equations with the FEM on adaptively refined meshes via parallelization

strategies has already been widely explored, see [42, 43, 44, 45, 46, 47] to cite but a few. A large set of these strategies lies on refinement-tree based partitioning methods and hence non-conforming h-adaptive approaches (with hanging nodes). In addition, it has been recently presented in [48] an algorithm for solving hanging-node constraints in the context of matrix-free FEM on central processing units (CPUs) and graphics processing units (GPUs). All these methods and algorithms have been integrated into several scalable open-source FEM libraries such as deal.II [49], MFEM [50], MoFEM [51], FEniCS [52], FreeFem++ [53] or libMesh [54] for example.

Addressing large-scale contact problems, adapted to the multiprocessor architecture of supercomputers, have been under study for many years. Indeed, pioneer works [55, 56, 57] introduce domain decomposition methods and associated iterative solution algorithms suitable to parallel computers. However, the performance of these methods has been shown on a small number of processes, no more than twenty or so. Penalty method applied on rigid-deformable contact problems [58] enables to reach good performances until sixty processors. Recent studies [59, 60, 61, 62, 63] propose strategies enabling scalable calculations on more processes. For these methods, the increase in solution accuracy (or in number of degrees of freedom) is based on uniform mesh refinement. Works detailed in [59, 60, 63] focus on saddlepoint problems (arising with Lagrange multipliers or mortar methods) with dedicated preconditioners. These approaches are scalable up to a few hundreds of cores. In [61, 62], parallel algorithms for rigid-deformable contact, scaling up to over 1,000 cores are described. The proposed strategies are based on domain decomposition methods (Dirichlet-Neumann or FETI like) for fulfilling contact conditions.

Combining the parallelization of AMR methods with contact mechanics remains a scientific challenge. As described before, current developments are mainly focusing either on non-parallelized adaptive methods for contact problems, or on parallelization methods for contact problems solved on uniformly refined meshes. To the best of our knowledge, only the study presented in [64] analyzes the parallel performance of solving a contact mechanics problem with adaptive local mesh refinement. A conventional one-body contact problem (rigid-deformable contact) is solved with a primal-dual active set strategy based on Lagrange multipliers that can be seen as a semi-smooth Newton method. This rigid-deformable contact problem greatly simplifies the general deformable-deformable contact problem, especially in terms of contact detection and mesh refinement. The strategy is implemented in the

deal.II FEM library. The mesh refinement is conducted by a variant of the Kelly error estimator [65], ready for use as part of deal.II. A hierarchical non-conforming h-adaptive refinement is then applied to linear and quadratic hexahedral finite elements. Contact simulation results with a scalability up to 1,024 processes are shown.

The aim of this paper is to introduce an HPC strategy for solving 3D elastostatic contact mechanics problems with AMR, and potentially curved contact boundaries. As said before, several software environments combining HPC and AMR in a FEM framework already exist. We then decided to add contact mechanics treatment in such environment. The MFEM software environment was chosen for the following main reasons: proven scalability to large numbers of cores, mature support for hexahedrons and tetrahedrons, support for non-conforming AMR, a large active community, and the ability to be integrated into a software stack. Furthermore, the minimal set of tools that MFEM provides for modeling contact mechanics is valuable. It gave us the opportunity to develop and examine parallel solutions in more complex settings, as well as evaluate the performance of combining AMR and parallelism in such configurations.

The meshes being considered are based on quadrilateral/hexahedral finite These elements are attractive for their tensor-product structure [66, 67, 49], their better accuracy (compared to triangles or tetrahedra) for the same approximation space order [49], and offer great advantages for the majority of solid mechanics problems such as contact mechanics [31, 68]. A so-called hierarchical h-adaptive AMR strategy is applied [69, 70]. It consists in directly subdividing the elements in areas of interest while maintaining the same order of interpolation, contrary to p or hp-adaptive methods that induce an increase in the order of the elements. Mesh-step refinement techniques enable to obtain optimal convergence rates even for problems with geometrical singularities [71, 72] and are strongly featured in the solid mechanics community. In addition, hierarchical refinement generally leads to optimal refined meshes [69, 70, 73] with respect to the total number of degrees of freedom and allows better control of the adaptation process through an explicit hierarchical data structure. When using quad/hexa elements, this AMR approach leads to non-conforming meshes with hanging nodes [73] for which continuity must be ensured. In MFEM, a parallelized algorithm for non-conforming h-adaptive mesh refinement is already available [74] based on prolongation and restriction operators to solve the linear system on conforming nodes only. This ready for use mesh refinement technique is enriched

by estimate-mark-stop-refine procedures inspired by [73] where they proved their effectiveness in terms of number of mesh elements versus precision. They are mainly based on the Zienkiewicz-Zhu a posteriori estimator [30], already implemented in the MFEM library. This estimator is widely used in solid mechanics as it is generic (not confined to a specific problem), cheap to compute, easy to implement and works pretty well in practice [75]. In this study, only one error estimator is tested since our main objective is the introduction of a generic parallelized AMR strategy for contact mechanics and not an in-depth study of error estimators.

The combination of AMR and contact problems highlights the problems of hierarchically refined curved interfaces [32, 31, 40] in the FEM framework. In order to avoid hand-made procedures ensuring the potential contact nodes to be located on the curved boundary during the refinement process [31, 73], we propose to use super-parametric elements in order to preserve the shape of the initial geometry boundary, even for first-order finite element solutions. These are elements whose degree of interpolation of the geometry is greater than that of the basis functions of the solution.

In the present paper, the contact problem is handled by a penalization algorithm. This enables one to deal with primal variables only: it provides a way for modelling the phenomenon under study while not increasing the number of unknowns (as it could be using Lagrange multipliers) and not modifying the formulation in an intrusive manner (as it could be using Nitsche's method). In addition, parallelized operators for solving constrained systems available in MFEM can be directly employed. Let us underline that providing scalable solvers and associated preconditioners for saddle-point problems is still a ongoing work [59, 63, 76], which supports our choice of the penalty method. An in-depth study around the penalty coefficient in order to limit interpenetration while controlling the computational time is carried out in this paper. A node-to-node pairing combined to an active set strategy [77] is applied for the detection of elements in contact. Although it may seem limiting, this node pairing strategy remains of interest nowadays for its good modeling properties [78, 79]. Its combination with automatic mesh refinement makes it possible to consider its use in the case of small tangential slip. Finally, the combined AMR-contact algorithm is ruled by two nested iterative loops. The external loop concerns the AMR process while the internal one deals with the contact solution.

The proposed scalable contact algorithm is based on a mesh partitioning strategy that ensures the contact paired nodes to be on the same MPI process. Hence, the algorithm building the local contact stiffness matrix does not depend on communications with other processes. As a result, communication overheads are reduced and the code is considerably simplified. In practice, the partitioning of the mesh is governed by an algorithm that guarantees the load equidistribution across processes, and that respects the distribution constraint related to the paired contact nodes mentioned above. This partitioning strategy offers a straightforward implementation, as it does not consider the spatial vicinity of elements within the solid when assigning them to processes.

The scalability of the developed AMR-contact algorithm and its main functions are analyzed in this article. It should be noted that mesh coarsening and mesh adaptation over time are beyond the scope of this article and will be considered in future studies.

The rest of the paper is organized as follows. Section 2 recalls the contact mechanics problem between deformable bodies and presents the main ingredients of the chosen solution algorithm. Section 3 is devoted to the adaptive mesh refinement strategy, focusing on special insights for contact mechanics. The extension of the considered AMR-contact algorithm to parallel settings is described in Section 4. Various numerical and performance studies carried out on the Hertzian elastostatic contact problem (in 2D and 3D) are reported and discussed in Section 5. Finally, some concluding remarks are provided.

#### 2. Contact modeling

#### 2.1. Governing equations

Two linearly elastic solids  $\Omega^s(s=1,2) \subset \mathbb{R}^m$  (with m the space dimension) are considered in frictionless contact on  $\Gamma_C^s$ , the potential contact boundaries. A schematic representation of the problem is given in Figure 1.

In  $\Omega = \Omega^1 \cup \Omega^2$  (such that  $\Omega^1 \cap \Omega^2 = \emptyset$ ), the considered elastostatic frictionless unilateral contact problem with infinitesimal strain assumption writes

$$(\mathcal{P}): \begin{cases} -\operatorname{div}\boldsymbol{\sigma}\left(\mathbf{u}\right) = \mathbf{0} & \text{in } \Omega \\ \boldsymbol{\varepsilon}\left(\mathbf{u}\right) = \frac{1}{2}\left(\nabla\mathbf{u} + \nabla\mathbf{u}^{T}\right) & \text{in } \Omega \\ \boldsymbol{\sigma}\left(\mathbf{u}\right) = \mathbf{C}: \boldsymbol{\varepsilon}\left(\mathbf{u}\right) & \text{in } \Omega \\ \text{Boundary conditions} & \text{on } \Gamma_{BC} \\ \text{Contact condition} & \text{on } \Gamma_{C}. \end{cases}$$

$$(1)$$

with **u** the problem's solution in displacement,  $\sigma$  and  $\varepsilon$  the stress and strain tensors respectively, and **C** the fourth order elasticity tensor.

Boundaries 
$$\Gamma_{BC}$$
 and  $\Gamma_{C}$  are defined such as
$$\begin{cases}
\Gamma_{BC} \cup \Gamma_{C} = \partial \Omega \text{ (boundary of } \Omega) \\
\Gamma_{BC} \cap \Gamma_{C} = \emptyset \\
\Gamma_{BC} = \Gamma_{BC}^{1} \cup \Gamma_{BC}^{2} \\
\Gamma_{C} = \Gamma_{C}^{1} \cup \Gamma_{C}^{2}.
\end{cases}$$

Classical boundary conditions (Dirichlet or Neumann) are applied on  $\Gamma_{BC}$  so that the Problem  $(\mathcal{P})$  is well-posed.

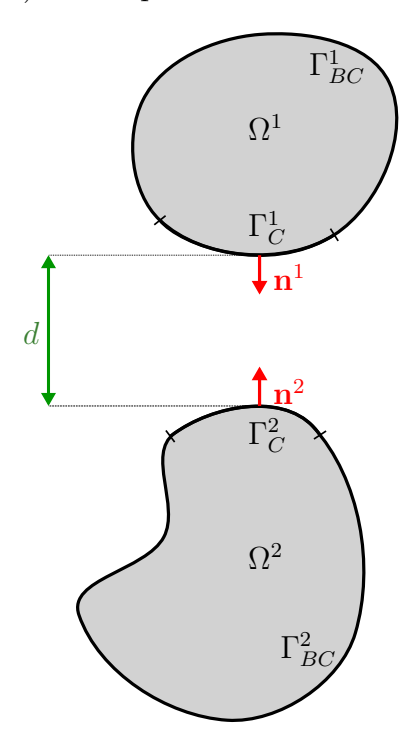


Figure 1: Sketch of the contact problem.

In the common contact mechanics theory, Signorini contact conditions (see [80, 81]) are prescribed on  $\Gamma_C$ , see Eq. (2).

$$\begin{cases} u_N - d \le 0 & \text{(non penetration)} \\ \sigma_N \le 0 & \text{(non adhesion)} & \text{on } \Gamma_C \\ \sigma_N (u_N - d) = 0 & \text{(complementarity)} \end{cases}$$
 (2)

with  $u_N = \mathbf{u}^1 \cdot \mathbf{n}^1 + \mathbf{u}^2 \cdot \mathbf{n}^2$  the normal displacement,  $\sigma_N = (\boldsymbol{\sigma}^1 \cdot \mathbf{n}^1) \cdot \mathbf{n}^1 = (\boldsymbol{\sigma}^2 \cdot \mathbf{n}^2) \cdot \mathbf{n}^2$  the normal contact stress and d the initial distance (gap) between

solids. We denote by  $\mathbf{u}^s$  the displacement field in  $\Omega^s$ :  $\mathbf{u}^s = \mathbf{u}|_{\Omega^s}$ , and by  $\boldsymbol{\sigma}^s$  the stress field in  $\Omega^s$ :  $\boldsymbol{\sigma}^s = \boldsymbol{\sigma}|_{\Omega^s}$ . The symbol '·' indicates the inner product, while  $\mathbf{n}^s$  represents the external unit normal to  $\Omega^s$  on  $\Gamma_C^s$ . Moreover, the framework of the infinitesimal strain theory implies that  $\mathbf{n} = \mathbf{n}^1 = -\mathbf{n}^2$ .

Conditions (2), graphically represented in Figure 2a in contact forces  $F_N$ , make the contact problem highly non-smooth and non-linear.

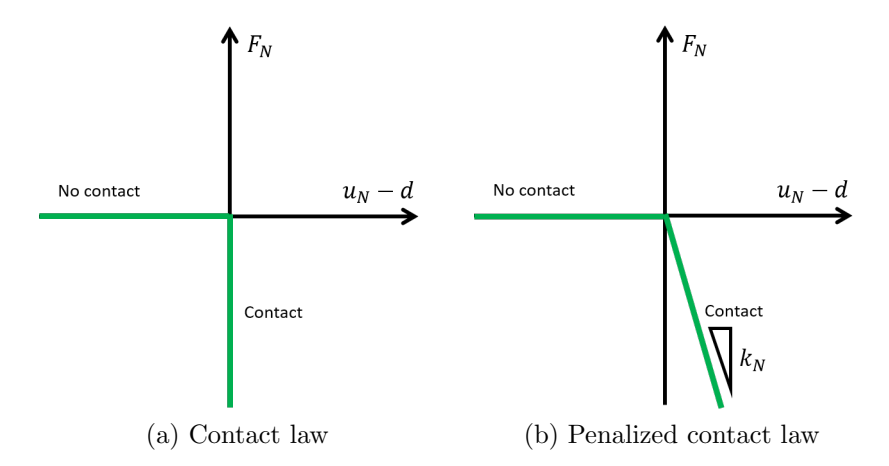


Figure 2: Illustration of contact and penalized contact laws.

#### 2.2. Discrete form

A generic contact mechanics problem in discrete form can be written as

$$(\mathcal{P}'): \begin{cases} \mathbf{L}^{int}\left(\mathbf{U}\right) - \mathbf{L}^{ext} - \mathbf{L}^{C}\left(\mathbf{U}\right) &= \mathbf{0} \\ \mathbf{B}\mathbf{U} &\leq \mathbf{D} \end{cases}, \tag{3}$$

where **U** denotes the discrete displacement solution, while  $\mathbf{L}^{int}$ ,  $\mathbf{L}^{ext}$  and  $\mathbf{L}^{C}$  denote the internal, external and contact forces operators respectively. In addition, **B** is the pairing matrix of potential contact nodes used to define the discrete relative displacements and **D** the initial gaps between the paired nodes.

Hence in Eq. (3), the ' $\leq$ ' symbol is used to represent the componentwise inequality.

**Remark:** The term  $\mathbf{L}^{C}(\mathbf{U})$  should be understood in a general sense. When applying the Lagrange multipliers method or one of its variants

(augmented Lagrangian, mortar,...), the dependence on **U** is replaced by a dependence on the additional variable associated with the method.

In the elastostatic case under consideration, the internal forces reduce to

$$\mathbf{L}^{int}(\mathbf{U}) = \mathbf{K}\mathbf{U},\tag{4}$$

with  $\mathbf{K}$  the stiffness matrix.

The penalty method consists in rewriting the contact inequality problem (3) as a variational equality, much easier to solve by classical solvers. This is done by identifying the set of active contact conditions, denoted  $\mathcal{A}$ , which is defined by Equation (5).

$$\mathcal{A} = \{ i \in [1; N_C] ; \sum_{j=1}^{N} \mathbf{B}_{ij} \mathbf{U}_j \ge \mathbf{D}_i \}$$
 (5)

with N the number of (primal) degrees of freedom, and  $N_C$  the number of potential contacts.

As the matrix **B** is defined only on the degrees of freedom located the potential contact boundary  $\Gamma_C$ , the sum in Eq. 5 is practically restricted to the primal nodes belonging to the set  $\mathcal{A}_c$ 

$$\mathcal{A}_c = \{ j \in [1; N] ; \exists i \in [1; N_C] \text{ such that } \mathbf{B}_{ij} \neq 0 \}.$$

Then, the active pairing matrix  $\hat{\mathbf{B}}$  is obtained by restricting the rows of  $\mathbf{B}$  to the set  $\mathcal{A}$ , see Eq. (6). The 'active' gap vector  $\hat{\mathbf{D}}$  is defined similarly, see Eq. (6).

$$\begin{cases} \hat{\mathbf{B}} &= \mathbf{B} \left[ \mathcal{A} \right] \\ \hat{\mathbf{D}} &= \mathbf{D} \left[ \mathcal{A} \right] \end{cases}$$
 (6)

The contact reaction force is defined in order to penalize surface interpenetration. By the way, the contact formulation is regularized, see Figure 2b, and the discrete penalized contact forces  $\mathbf{L}^{C}(\mathbf{U})$  are given by Eq. (7).

$$\mathbf{L}^{C}(\mathbf{U}) = k_{N}\hat{\mathbf{B}}^{T} \left(\hat{\mathbf{D}} - \hat{\mathbf{B}}\mathbf{U}\right) \tag{7}$$

with  $k_N \gg 1~\rm N.m^{-1}$  the penalty coefficient, which can be interpreted as a spring stiffness in the contact interface, see [2]. Finally the mechanical equilibrium writes

$$\left(\mathbf{K} + k_N \hat{\mathbf{K}}_C\right) \mathbf{U} = \mathbf{L}^{ext} + k_N \hat{\mathbf{B}}^T \hat{\mathbf{D}}$$
(8)

with 
$$\hat{\mathbf{K}}_C = \hat{\mathbf{B}}^T \hat{\mathbf{B}}$$
.

As mentioned in the introduction, Problem (8) only involves primal unknowns. On the other hand, with this penalty approach, interpenetration between solids is allowed [2], since this is the driving term of the contact force.

The mfem::PenaltyConstrainedSolver class of the MFEM software fully forms the linear system (8) from penalty coefficient  $k_N$ , matrices and vectors  $\mathbf{K}$ ,  $\hat{\mathbf{B}}$ ,  $\mathbf{L}^{ext}$ ,  $\hat{\mathbf{D}}$  provided as input.

### 2.3. Node-to-node pairing

To solve the contact problem described by Equation (8), a preliminary step which consists in pairing potential contact nodes is required. Indeed, this step enables to build the matrix  $\mathbf{B}$  and the vector  $\mathbf{D}$ , from the positions of the mesh nodes located on the contact boundaries of the solids. The process consists in pairing the closest potential contact nodes using a position criterion.

In computational contact mechanics, there are many ways to pair the contact interface nodes. The most common are the node-to-node, node-to-surface and surface-to-surface pairing algorithms. Here, the node-to-node pairing approach is chosen for its ease of implementation and very low calculation costs. However, it restricts the problem and the geometry to be taken into account. The initial meshes must have matching contact interfaces. Moreover, this pairing approach is only valid under infinitesimal strain theory and infinitesimal sliding, so that the potential contact nodes always face each other.

Thus, the MFEM software is enriched with our own node-to-node pairing algorithm which consists in finding, for each node of the first solid, the nearest node of the second solid in the direction of the (a priori given) contact outward normal.

#### 2.4. Algorithmic treatment of the penalized contact problem

The proposed algorithm for solving the contact problem is ruled by an iterative process, see Algorithm 1. Node-to-node pairing is performed before entering the loop, whereas the set of active contact pairs of nodes  $\mathcal{A}$  is updated at the end of each iteration thanks to an active set algorithm (see [77] for example) by looking at the interpenetration between the solids, see Definition (5). The set of active contact nodes may vary at each iteration, and

the contact matrix and vector,  $\hat{\mathbf{K}}_C$  and  $\hat{\mathbf{B}}^T\hat{\mathbf{D}}$  respectively, are reconstructed accordingly. The resulting linear system, see Eq. (8), is typically solved by a preconditioned conjugate gradient (PCG) linear iterative solver, suitable for penalized problems resulting in large sparse symmetric positive-definite systems. The stopping criterion of the contact solution process requires that the set of active contact nodes no longer varies in iteration.

# Algorithm 1 Contact solution process

```
Input: Data of the problem, maximum number of contact loop
iterations l_{max}
Output: Finite element solution U
Initialization
  Process the node-to-node pairing
  Initialize contact loop parameters: l \leftarrow 1, stop_C \leftarrow false
  Define the initial set of active contact nodes (if any)
while (stop_C = false \text{ and } l \leq l_{max}) \text{ do}
 Form penalized linear system
 Solve the linear system
 Define the new set of active contact conditions
 if no evolution of the active contact set then
   stop_C \leftarrow true
 else
  l \leftarrow l + 1
 end if
end while
```

#### 3. Adaptive mesh refinement process

The non-conforming h-adaptive strategy is performed using an iterative algorithm described in Figure 3. The problem is first solved on a coarse (generally conforming) mesh before applying the refinement process according to a chosen detection criterion. This process, called ESTIMATE-MARK-REFINE strategy [21, 82, 73], is iteratively repeated until a stopping criterion is satisfied.

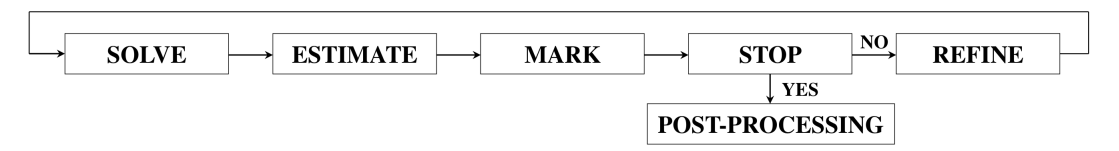


Figure 3: Generic adaptive mesh refinement algorithm, figure from [73].

In the following sections, the main points of each module of the AMR algorithm are described.

#### 3.1. Error estimation: module ESTIMATE

The key ingredient for automatic mesh adaptation is the error estimator. Since the present study does not aim at comparing the efficiency of error estimators, the Zienkiewicz and Zhu [30] a posteriori error estimator is set as the tool for driving mesh refinement. This estimator is based on the difference between a smoothed stress field  $\sigma^*$  and the finite element one  $\sigma^h$ , which is, for a displacement-based solution, generally discontinuous between elements. For the construction of the smoothed field, the nodal projection technique introduced in [30] is performed. Assuming that  $\Omega^h$  is the quadrangulation of  $\Omega$ , each mesh element is denoted  $T_i, i \in [1; N_E]$  such that  $\overline{\Omega^h} = \bigcup_i^{N_E} \overline{T_i}$ . Hence  $N_E$  represents the total number of element of the mesh. The local element-wise error in the energy norm writes for a mesh element  $T_i$ :

$$\xi_{T_i} = \left( \int_{T_i} \left( \boldsymbol{\sigma}^* - \boldsymbol{\sigma}^h \right) : \left( \boldsymbol{\varepsilon}^* - \boldsymbol{\varepsilon}^h \right) dT_i \right)^{1/2}. \tag{9}$$

<u>Remark:</u> In practice, this integral is evaluated at integration points where  $\sigma^h$  is defined.

As proposed in [31], this classical projection-based ZZ estimator [30] is applied in each solid independently without any other modification. The global absolute estimated error on  $\Omega^h$  is then written by summing the elementary contributions

$$\xi_{\Omega} = \left(\sum_{T_i \in \Omega^h} \xi_{T_i}^2\right)^{1/2}.\tag{10}$$

In the MFEM software library, the element-wise error distribution  $\{\xi_{T_i}\}_{T_i\in\Omega^h}$  are computed using the GetLocalErrors function applied to the mfem::ZienkiewiczZhuEstimator error estimator. The scalar value  $\xi_{\Omega}$  is then obtained from the element-wise field  $\{\xi_{T_i}\}_{T_i\in\Omega^h}$  thanks to the GetNorm function.

# 3.2. Marking stage: module MARK

# 3.2.1. Mesh optimality criteria: sub-module OPTIMALITY

The strategy for selecting the elements to be refined is basically based on a qualitative use of the estimated element-wise error field. Qualitative approaches involve an empirical detection of the elements to be refined. The best-known are quantile marking, Dörfler marking or maximum marking, see [83] for further details. In this case, the optimal choice of the required parameters is not obvious, since these parameters are not directly linked to a desired accuracy and may depend on the problem under consideration, see [84, 85] for example.

In our developments, we prefer to rely on quantitative marking approaches, related to an user-prescribed accuracy. To this end, a maximum permissible element-wise error, denoted  $\xi_{T_i}^{\text{max}}$ , has to be defined. Two mesh optimality criteria, focusing either on a global or local error, are studied.

# • ZZ criterion: equidistribution of the specific error.

In [30], Zienkiewicz and Zhu proposed a mesh optimality criterion based on principle of error equidistribution:

$$\xi_{T_i}^{\max, ZZ} = \text{const} \quad \forall T_i \in \Omega^h.$$
 (11)

The global absolute estimated error on  $\Omega^h$  is then defined by

$$\xi_{\Omega}^{\text{max,ZZ}} = e_{\Omega} \omega_{\Omega} = \sqrt{N_E} \, \xi_{T_i}^{\text{max,ZZ}} \tag{12}$$

with  $N_E$  the number of mesh elements,  $e_{\Omega}$  the user-prescribed accuracy and  $\omega_{\Omega}$  the energy norm associated to the global strain. This value is obtained by summing the elementary contributions:

$$\omega_{\Omega} = \left(\sum_{T_i \in \Omega^h} \omega_{T_i}^2\right)^{1/2} \tag{13}$$

where the strain energy  $\omega_{T_i}^2$  on element  $T_i$ , introduced in [30], is given by

$$\omega_{T_i}^2 = \int_{T_i} \boldsymbol{\sigma}^h : \boldsymbol{\varepsilon}^h dT_i + \int_{T_i} \left( \boldsymbol{\sigma}^* - \boldsymbol{\sigma}^h \right) : \left( \boldsymbol{\varepsilon}^* - \boldsymbol{\varepsilon}^h \right) dT_i \ \forall \ T_i \in \Omega^h.$$
 (14)

Thus, the maximum permissible absolute element-wise error is then defined by

$$\xi_{T_i}^{\text{max,ZZ}} = e_{\Omega} \frac{\omega_{\Omega}}{\sqrt{N_E}}.$$
 (15)

Criterion (15) is the most widespread mesh optimality criterion known to date.

#### • LOC criterion: local element-wise error.

In [85], a local optimality criterion (LOC) is introduced and has been shown in [73] to be more reliable for local error control in the framework of structural mechanics problems. In addition, this criterion has been evaluated in [31] for contact problems. The maximal permissible element-wise error distribution is directly governed by the admissible local element-wise error:

$$\xi_{T_i}^{\text{max,LOC}} = e_{\Omega,\text{LOC}} \,\omega_{T_i}. \tag{16}$$

As proved in [85], this automatically implies the relative global error to be bounded above by  $e_{\Omega,LOC}$ .

In the MFEM software library, the mfem::MeshOperator::ApplyImpl function dedicated to the elements marking for refinement has been enriched with implementations required to evaluate the maximal permissible errors: calculations of  $\omega_{T_i}$ ,  $\omega_{\Omega}$ , and, a fortiori,  $\xi_{T_i}^{\max,ZZ}$  and  $\xi_{T_i}^{\max,LOC}$ .

#### 3.2.2. Detect elements: sub-module DETECT

From the maximum permissible element-wise error, the set of marked elements is simply defined by

$$\mathcal{M}^0 = \left\{ T_i \in \Omega^h / \xi_{T_i} > \xi_{T_i}^{\text{max}} \right\}. \tag{17}$$

In order to garantee the refined contact boundaries to remain matched (required for the node-to-node contact pairing), the  $\mathcal{M}^0$  set has to be enlarged. Elements located on the potential contact boundaries whose paired element is marked for refinement, are then also marked for refinement as proposed in [31].

$$\mathcal{M} = \mathcal{M}^0 \cup \{T_j \in \Omega^h / T_i \in \mathcal{M}^0 \text{ paired with } T_j\}.$$
 (18)

Here, we define finite elements as paired when all their nodes located on contact boundaries are each other paired.

To that end, the MFEM mfem::MeshOperator::ApplyImpl function has been enriched to receive paired elements as input.

# 3.3. Stopping criteria: module STOP

The AMR process obviously stops when the set of marked elements becomes empty:

$$\mathcal{M} = \emptyset. \tag{19}$$

However, for problems with singularities, such as contact mechanics ones, criterion (19) may never be reached and infinite refinement in very localized zones may be performed. Other stopping criteria are therefore commonly added, allowing the refinement process to be ended once the mesh is considered as acceptable.

In this study, we may be interested in verifying either global or local accuracies. The refinement process is therefore analyzed using two stopping criteria.

# • Global stopping criterion.

The stopping criterion most commonly used in the literature is a global criterion based on the estimated absolute global error, see Eq. (20).

$$\frac{\xi_{\Omega}}{e_{\Omega}\omega_{\Omega}} \le 1. \tag{20}$$

#### • Local stopping criterion.

When the control of the local error is of interest (see detection criterion (16)), a local stopping criterion, introduced in [85] and based on geometric considerations, is used to stop the refinement process. Indeed, the respect of the global stopping criterion (20) does not guarantee any precision at local level. The local stopping criterion, see Eq. (21), ensures that the measure of the set of detected elements  $\mathcal{M}$  is below a proportion ( $\delta$ ) of the total measure of the domain.

$$\mu\left(\Omega_{\mathcal{M}}\right) \le \delta \cdot \mu\left(\Omega^{h}\right) \tag{21}$$

with  $\mu(\Omega_{\mathcal{M}})$  the measure of detected area  $\overline{\Omega_{\mathcal{M}}} = \{ \cup \overline{T_i} / T_i \in \mathcal{M} \}, \ \mu(\Omega^h)$  the measure of global mesh, and  $\delta$  the user-defined local error control parameter.

With this stopping criterion, the obtained solution satisfies the local optimality criterion (16) over  $(1 - \delta) \times 100$  percent of the domain. This local stopping criterion therefore has the advantage of automatically determining a discrete approximation of the critical area in the presence of contact singularities, which is of great interest.

**Remark:** Setting  $\delta = 0$  makes the criterion equal to (19). In addition, choosing  $\delta \ll 1$  prevents a rough representation of the critical area.

## 3.4. Mesh refinement: module REFINE

The mesh refinement is based on an isotropic hierarchical refinement, consisting in dividing each marked quad/hexa element (also called parent element) in  $2^m$  (with m the space dimension) sub-elements of the same type (also called child elements), based on splitting each side into 2 equal parts. The refinement ratio is chosen to be equal to 2 according to the study conducted in [73].

In addition, the 'single irregularity rule' (also called 'single hanging node rule' or '2:1 balance rule'), argued in [82, 73] for example and widely used in the literature, is applied. This has the effect of limiting to one the number of irregular nodes on each edge.

However for first-order finite elements, this hierarchical mesh refinement limits the geometry representation when considering curved boundary, which is generally the case of contact boundaries. In the literature (see [31, 73] for example), hand-made 'quasi-hierarchical' mesh refinement procedures have been proposed. They mainly consist of updating the discretization of the curved boundary by moving the nodes added by refinement onto the exact curved geometry, see Figure 4. This procedure gives very satisfactory results, but is intrusive and not generic as it requires knowledge of the closed-form equation of the curved boundary during the refinement step.

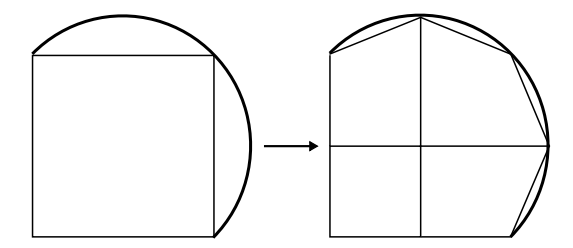


Figure 4: Quasi-hierarchical isotropic mesh refinement.

In this contribution, shape preservation of hierarchically refined geometries is automatically guaranteed by the use of super-parametric finite elements. These elements are based on a geometric transformation of higher degree of interpolation than the solution's basis functions. With this type of element, the surface approximation error during refinement can be very low compared to the one obtained with a first-order transformation, see Figure 5.

These elements are therefore ideally suited to contact mechanics problems where the active contact zone must be charactized precisely.

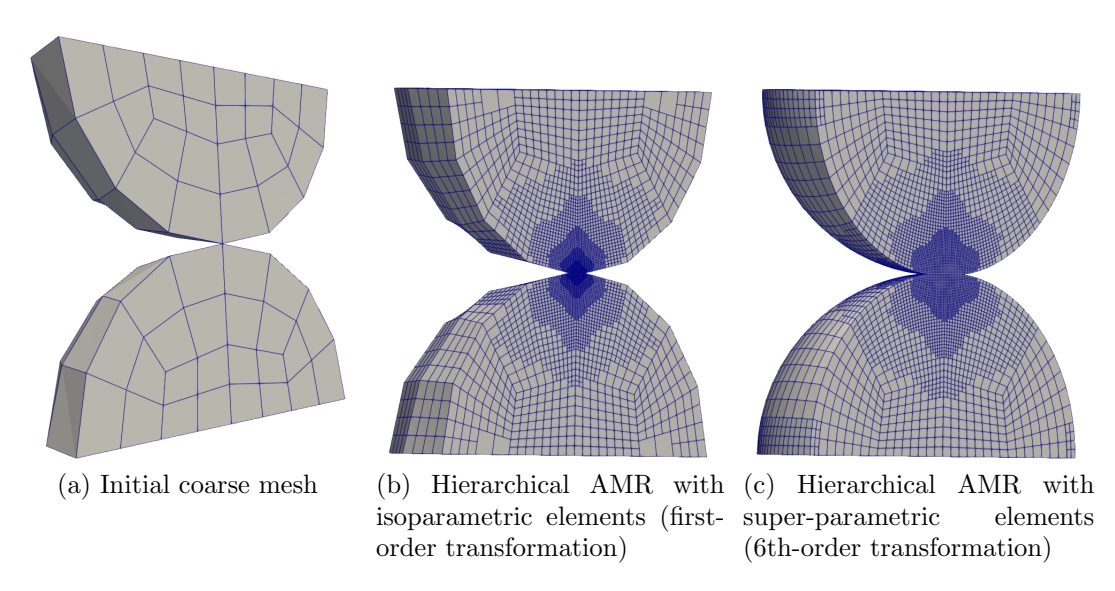


Figure 5: Hierarchical AMR for curved-edge contact problem with first-order finite element solution: isoparametric versus super-parametric elements.

This type of super-parametric element is defined during the mesh design phase and is properly supported by the MFEM software environment. As a result, the discrete geometry does not need to be updated during the refinement process.

The MFEM refinement procedure, named mfem::MeshOperator::Apply, is invoked to carry out the chosen non-conforming h-adaptive mesh refinement strategy [74, 50]. The single irregularity rule is activated by setting the nc\_limit parameter to 1.

#### 3.5. Non-conforming solution: module SOLVE

Refinement of a quadrangular or hexahedral elements mesh using the hierarchical h-adaptive method results in the appearance of hanging nodes, see Figure 6. Thus, the non-conforming degrees of freedom (DOFs) must be constrained in order to obtain a conforming solution.

The major task in the use of this type of refinement method is to build the linear system to be inverted. The choice made in MFEM and detailed in [74] is to define (and solve) a problem restricted to conforming DOFs only.

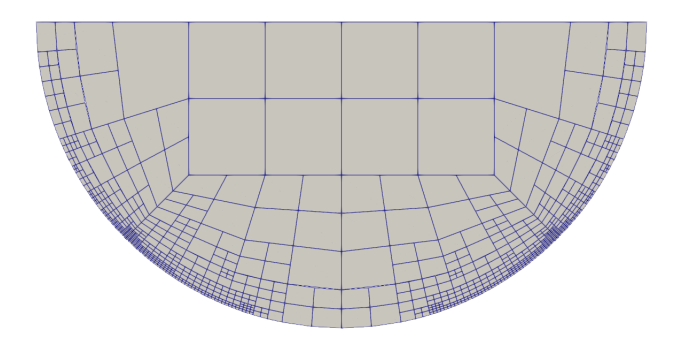


Figure 6: Example of a non-conforming h-adaptive refined mesh.

Its principle is recalled here after in order to present its extension to contact problems.

The global stiffness matrix (bilinear form)  $\tilde{\mathbf{K}}$  and the load vector of the linear finite element system  $\tilde{\mathbf{L}}^{ext}$  are assembled taking into account all the mesh nodes, without worrying about non-conformities. Thus, the resulting linear system writes

$$\tilde{\mathbf{K}}\tilde{\mathbf{U}} = \tilde{\mathbf{L}}^{ext} \tag{22}$$

with  $\tilde{\mathbf{U}}$  the vector containing all DOFs.

In order to restrict this system to conforming DOFs, a prolongation operator **P** is built:

$$\mathbf{P} = \begin{pmatrix} \mathbf{Id} \\ \mathbf{W} \end{pmatrix} \tag{23}$$

with **Id** the identity matrix and **W** the so-called interpolation matrix. This interpolation matrix **W** expresses the non-conforming DOFs to be constrained as linear combinations of the conforming DOFs using the finite element basis functions (see [74, 50] for further details on the procedure for building these matrices). Hence, we have

$$\tilde{\mathbf{U}} = \mathbf{P}\mathbf{U} \tag{24}$$

with U the conforming DOFs. Similarly, the test functions are projected onto the conforming space thanks to the prolongation operator P. Then, the linear system (22) becomes

$$\mathbf{P}^T \tilde{\mathbf{K}} \mathbf{P} \mathbf{U} = \mathbf{P}^T \tilde{\mathbf{L}}^{ext}.$$
 (25)

By defining the conforming stiffness matrix

$$\mathbf{K} = \mathbf{P}^T \tilde{\mathbf{K}} \mathbf{P},\tag{26}$$

and the conforming load vector

$$\mathbf{L}^{ext} = \mathbf{P}^T \tilde{\mathbf{L}}^{ext},\tag{27}$$

the linear system to be solved to obtain the solution U on conforming DOFs writes

$$\mathbf{KU} = \mathbf{L}^{ext}.\tag{28}$$

Once the finite element solution **U** is found, it is extended to all DOFs of the mesh through the prolongation operation (24).

The same projection operations need to be performed on the contact terms appearing in the penalized linear system (8). As said in Section 2.2, we have chosen to rely on the mfem::PenaltyConstrainedSolver class of MFEM which works on matrices and vectors associated to conforming DOFs. To this end, it is sufficient to define the active contact pairing matrix on conforming DOFs by with

$$\hat{\mathbf{B}} = \tilde{\mathbf{B}}[\mathcal{A}]\mathbf{P} \tag{29}$$

where  $\tilde{\mathbf{B}}$  is the potential contact pairing matrix assembled taking account all the DOFs, and  $\mathcal{A}$  the set of active contact nodes, see Section 2.2.

Then, the contact stiffness matrix built by the mfem::PenaltyConstrainedSolver class writes

$$\hat{\mathbf{K}}_C = \mathbf{P}^T \tilde{\mathbf{B}} [\mathcal{A}]^T \tilde{\mathbf{B}} [\mathcal{A}] \mathbf{P}, \tag{30}$$

which correspond to the projection to conforming DOFs of the global contact stiffness matrix  $\tilde{\mathbf{K}}_C = \tilde{\mathbf{B}}[\mathcal{A}]^T \tilde{\mathbf{B}}[\mathcal{A}]$ . The projection of the contact right-hand term is also consistent:

$$\hat{\mathbf{B}}^T \hat{\mathbf{D}} = \mathbf{P}^T \tilde{\mathbf{B}} [\mathcal{A}]^T \hat{\mathbf{D}}.$$
 (31)

Hence the contact right hand term  $\mathbf{D}$  given of input of PenaltyConstrainedSolver is directly

$$\hat{\mathbf{D}} = \tilde{\mathbf{D}}[\mathcal{A}]. \tag{32}$$

It should be noted that these algebraic operations are not directly available in MFEM classes and have been implemented specifically.

#### 3.6. Algorithmic treatment of the AMR-Contact solution process

The proposed AMR-Contact solution process is ruled by two nested iterative loops, described in Algorithm 2. This algorithm calls Algorithm 1 in which the definition of the initial set of active contact nodes is generally performed considering the solution at the previous AMR iteration (for computational efficiency).

# Algorithm 2 Combined AMR-Contact solution process

Rebalance the mesh partitioning (see Section 4.2)

```
Input: Data of the problem, maximum number of AMR loop
iterations n_{max}
Output: Finite element solution on non-conforming refined mesh
Initialization
  n \leftarrow 1, \, \textit{stop}_{\textit{AMR}} \leftarrow false
while stop_{AMR} = false and n \leq n_{max} do
 Assemble the bilinear and linear forms
 Restriction step.
   Form the conforming linear system
 Perform the contact solution process (SOLVE): call Algorithm 1
 Prolongation step.
   Reconstruction of the finite element solution on all DOFs
 Detect elements to be refined (ESTIMATE-MARK)
 Update stop_{AMR} with the stopping criterion (STOP)
 if stop_{AMR} = false then
  Refine detected elements (REFINE):
    Create the new non-conforming refined mesh
```

#### 4. Parallel strategy

 $n \leftarrow n + 1$ 

end if end while

Since accurate prediction of contact mechanics problems with mesh adaptation generally requires a large number of elements and a large sparse system to solve, distributing tasks among processes is an important matter. With the need for parallel codes becoming increasingly important, algorithms have been implemented in finite element libraries such as MFEM for handling large

non-conforming meshes [50]. However, adapting them for addressing contact mechanics problems remains a challenging task. In this section, we describe a parallel solution that is dedicated to this type of problem. To this end, the most common distributed-memory parallel processing paradigm is considered, namely Message Passing Interface (MPI).

# 4.1. MFEM non-conforming mesh partitioning

An effective combination of contact mechanics and non-conforming hrefinement strategies in a distributed-memory parallel processing framework is based, first and foremost, on a relevant mesh partitioning. In the MFEM library, the standard type of partitioning is element-based, i.e. each element is assigned to one of the MPI process (see [74] for further details). The set of (finite) mesh elements is divided into R disjoint regions, where R is the number of MPI tasks. The data related to vertices, edges and faces at the boundary of each task's region are duplicated by adding ghost elements (copy of foreign elements that are owned by other MPI processes), so that each region can be treated as an isolated submesh and processed in parallel. The prolongation operator  $\mathbf{P}$  (see Eq. (23)) is extended to the processing of ghost DOFs so that the solution of the linear system, obtained after the solver step in the SOLVE module, concerns the non-ghost conforming DOFs only.

By default in the MFEM library, when the mesh is hierarchically refined, child elements are preassigned to their parent MPI task. In case of non-conforming h-adaptive refinement, imbalance between MPI processes occurs, and a rebalance of elements is worthwhile. The mfem::ParMesh::Rebalance function can be called to produce a new mesh partition. Used as such (without any argument), it corresponds to a black-box function that builds a partitioning solution based on the classic geometric Space-Filling Curve (SFC) method [86, 87] via Hilbert curves.

In the MFEM library, the embedded functions for creating mesh partitioning are not currently suited to contact mechanics problems. Indeed, if they are applied as such, the paired contact nodes have no guarantee to be on the same processes. Thus, the construction of the contact pairing matrix **B** would require, at least, extra MPI communications. In this paper, we present a specific strategy that provides a new partitioning function. Adapting the mesh partitioning functions proposed by MFEM to contact problems is a future task. On the other hand, MFEM's other main features (assembly, linear system formation, solving, etc.) are still used.

#### 4.2. Contact-based mesh partitioning algorithm

The dedicated algorithm proposed here guarantees a mesh partitioning whose the contact paired nodes are on the same processes during the refinement iterations. Practically, this involves that the construction of the local contact pairing matrix **B** does not depend on communications with other processes. Hence, contact stiffness matrices and load contact vectors are assembled locally on each MPI task, as if each region were treated as an isolated mesh by the sequential part of the code. This highly reduces the amount of inter-process communications during the refinement iterations, enhancing code reachability and parallel scalability.

**Remark:** to simplify the code writing, elements lying on potential contact boundaries are not handled by the same MPI processes than non-contact elements of the solids.

The partitioning algorithm is implemented in the sequential part of the code, i.e. without any communication between the MPI tasks. This algorithm is responsible for assigning each element to the MPI task to which it will belong once the rebalancing is carried out. Here, the proposed algorithm provides a mesh partition to the mfem::ParNCMesh::Rebalance function, which then accordingly redistributes the elements between the MPI tasks. The algorithm is designed to ensure that, once the mesh has been redistributed, the work load is as equal as possible between the processes handling the contact elements on the one hand, and the other tasks on the other hand.

After applying the AMR algorithm (and before rebalancing), MPI regions initially handling contact elements can contain contact and non-contact elements. Generally speaking, in our partitioning algorithm, the contact and non-contact elements of the MPI regions are treated separately. The formula

$$R_C = \left\lceil c \frac{N_{E,C}}{N_E} R \right\rceil \tag{33}$$

defines the number of MPI tasks processing contact elements. In this equation,  $N_{E,C}$  represents the (even) number of contact elements,  $N_E$  the total number of mesh elements (both after AMR iteration), R the total number of MPI processes, c > 0 an a priori given coefficient and  $\lceil x \rceil$  the ceiling function of the scalar x (smallest integer greater or equal to x). In this formula, choosing c > 1 will lead to have fewer elements on average on MPI tasks processing contact elements than on the rest of the MPI processes, and inversely for c < 1. In addition,  $R_C$  is reassessed at each mesh refinement iteration as  $N_{E,C}$  and  $N_E$  may have changed.

The result obtained with Equation (33) must be corrected in the following cases:

$$\begin{cases}
R_C = \frac{N_{E,C}}{2} & \text{if } R_C > \frac{N_{E,C}}{2} \\
R_C = R - 1 & \text{if } R_C \ge R \text{ and } N_E > N_{E,C}.
\end{cases}$$
(34)

The first criterion guarantees that there is at least one pair of contact elements per MPI task processing contact elements. The second criterion ensures that at least one MPI process is retained for processing non-contact elements. Obviously, if there are contact elements only, the second criterion does not occur.

Then, for each region r containing  $N_{E,r}$  elements, the  $N_{E,C,r}$  contact elements (with  $N_{E,C,r}=0$  in non-contact MPI regions) must be assigned to the  $R_C$  first MPI processes handling the contact elements, while the  $(N_{E,r}-N_{E,C,r})$  other elements must be assigned to the following  $(R-R_C)$  MPI tasks.

As the main feature of our mesh partitioning algorithm is to ensure paired nodes to be on the same MPI task, a special attention is devoted to the distribution of the contact elements. Thanks to the node-to-node pairing algorithm, the element-based mesh partitioning algorithm can work on contact paired elements (see definition in Section 3.2.2). Practically, in each MPI region r, the contact elements of the first solid are distributed (quite) equally according to their local number on the  $R_C$  first MPI processes. These elements are assigned locally to MPI processes via a strategy close to SFC method applied to contact elements only. However, it differs from this method in two notable points. Firstly, unlike the SFC method via Hilbert curve, which performs a global renumbering of elements in order to partition them, thereby inducing communications between MPI tasks, only the local numbering of elements is taken into account here for partitioning. Thus, no communication between MPI processes is necessary. Secondly, as for a region r, there could be fewer contact elements than MPI tasks processing the contact elements  $(N_{E,C,r}/2 < R_C)$ , the number of the starting process for partitioning is defined as  $r \mod R_C$  (with 'mod' the modulo) to avoid potential imbalances. The number of the ending process is then  $(r + N_{E,C,r}/2) \mod R_C$ . Then, the contact elements in the second solid are affected to the same MPI process than their paired element in the first solid.

Then, the remaining (non-contact) elements must be distributed in a balance way on the remaining subset of MPI tasks. This is done according to a routine based on element equidistribution similar to that applied for the contact elements of the first solid.

Finally, once this new partitioning has been produced, the MFEM mfem::ParNCMesh::RedistributeElements function, called within the mfem::ParNCMesh::Rebalance function, handles transferring elements between MPI tasks, while respecting the specified partitioning. In addition, in the proposed AMR-Contact solution strategy, the rebalancing step is performed at the end of each AMR iteration, as this is a low-cost step [74].

An example of a partitioning produced by our strategy is shown in Figure 7. In this example, a local mesh refinement step has been performed, and the elements (represented here by boxes) must be partitioned across 8 MPI tasks, which initially have a variable number of elements. At the current AMR iteration, there are 3 MPI tasks handling contact elements, which, after application of the refinement step, contain both contact elements and non-contact elements. In Figure 7, contact elements are grouped by paired contact elements, and only the local number of the contact element of the first solid is considered. In this way, a contact element of the second solid is no longer identified by its local number, but by the local number of the contact element of the first solid to which it is paired. Each grouping of contact elements characterizes a 'super-element' and is illustrated in green in Figure 7. Non-contact elements are shown in white.

In addition, at the current AMR iteration, there are also 5 MPI tasks handling non-contact elements, which, once the refinement step has been completed, contain obviously non-contact elements only. For each MPI process, the elements (or pairs of contact elements) are numbered locally, and their local number is defined at the top row of Figure 7. After applying Equation 33 and criteria 34,  $R_C$  will be (in this example) 2 at the next AMR iteration, and  $R-R_C$  will therefore be 6. The MPI tasks handling the contact elements will therefore be processes 0 and 1, while the processes handling the non-contact elements will be processes 2, 3, 4, 5, 6 and 7. The shift in the starting process number for partitioning is also highlighted with the partitioning example presented in the figure. Indeed, for each process, the process number assigned to the mesh element corresponding to the first green (respectively white) box starting from the left is given by r mod  $R_C$  (respectively r+ $R_C$  if r+ $R_C$  < R or r+ $R_C$  mod  $R-R_C$  otherwise, with 'mod' being the modulo operation): for example, the first white box of process 4

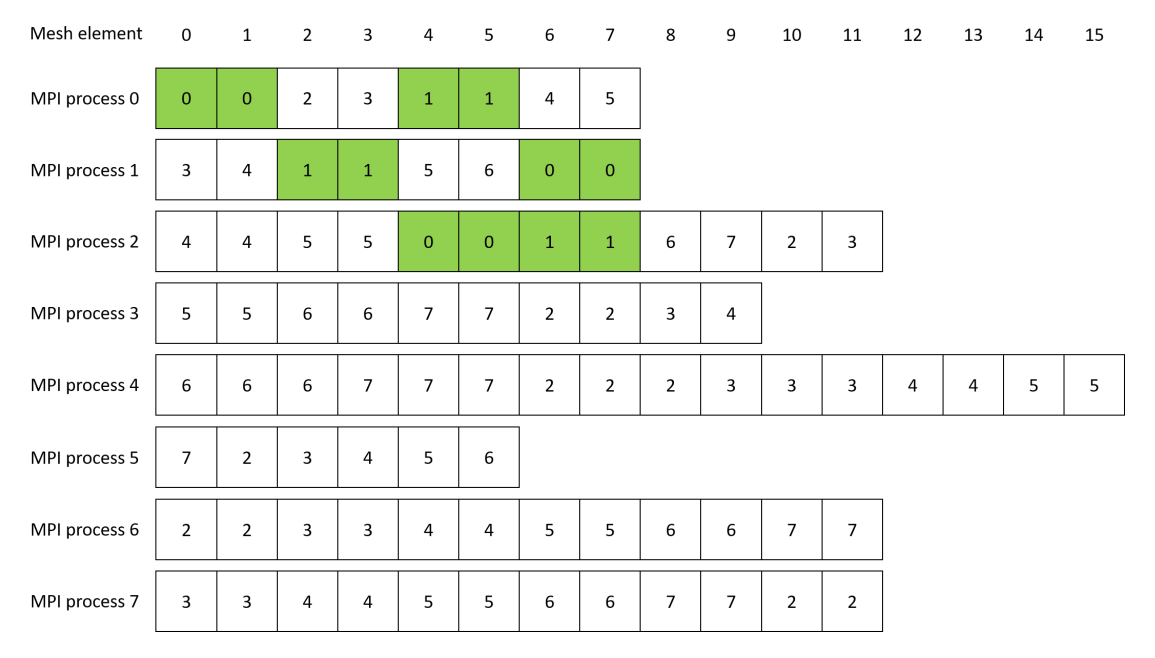


Figure 7: Illustration of the partitioning principle for 8 MPI processes. In green = 'super-elements', in white = non-contact elements. The number of boxes per process corresponds to the number of 'super-elements' and non-contact elements that the processes have after applying AMR and before rebalancing the elements. The number in each cell specifies the process number to which the contact 'super-element' or the non-contact element will be assigned.

has been assigned the number 6 and that of process 5 has been assigned the number 7. Similarly, this figure allows us to observe that the end process number (for contact elements:  $(r + N_{E,C,r}/2) \mod R_C$ ; for non-contact elements:  $r + R_C + N_{E,\bar{C},r}$  if  $r + R_C + N_{E,\bar{C},r} < R$  or  $r + R_C + N_{E,\bar{C},r} \mod R - R_C$  otherwise) differs depending on the process considered (and the number of elements it has to redistribute). For example, for the contact elements of process 1, the end process is 0, and for the non-contact elements of process 4, the end process is 5.

Furthermore, it should be noted that the case where  $N_{E,C,r}/2 < R_C$  (which would mean that the number of green boxes is strictly less than  $R_C$ ) does not happen in the example proposed here. Indeed, for each process with contact elements (initially MPI rank = 0, 1, 2), the number of green cells is greater than  $R_C = 2$ .

Then, the proposed partitioning algorithm provides a new local partition

of the mesh which is that given in Figure 7, where the number inscribed in each box indicates the MPI process to which the element (or pair of contact elements) is newly assigned.

Applying the proposed strategy to the example presented in Figure 7 leads to the mesh partitioning illustrated on 2D meshes in Figure 8b. The initial partitioning is reported on Figure 8a

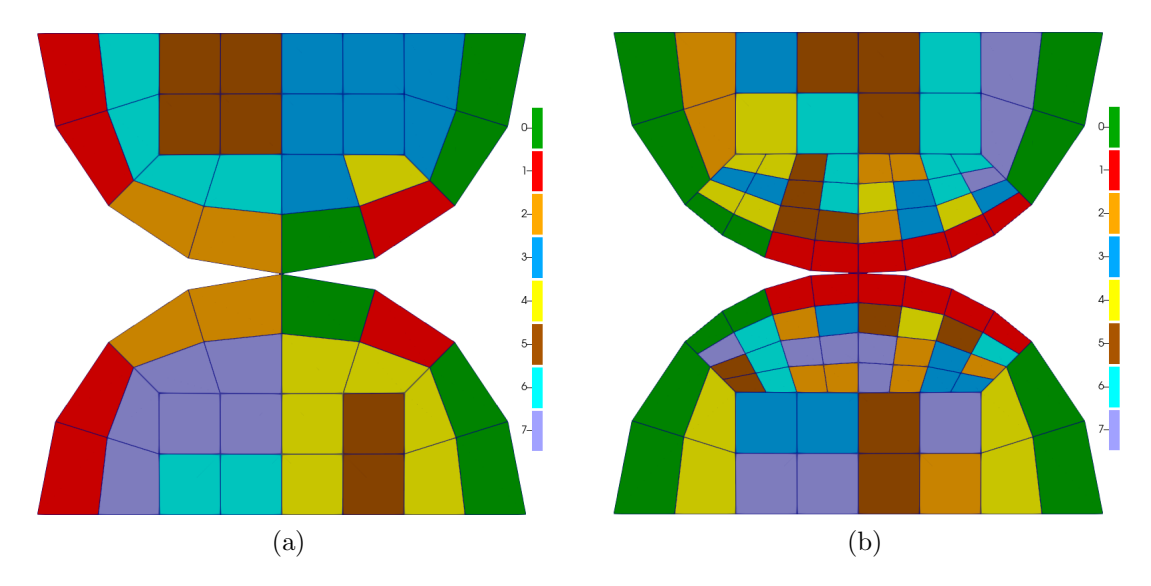


Figure 8: Contact-based load balancing illustration for a 2D mesh, typical of the Hertzian problem - Each color identifies a specific MPI task - Mesh partitionings at first and second AMR iteration in (a) and (b) respectively.

This figure displays the MPI task numbers assigned to the elements of a 2D mesh used for an contact simulation with AMR (here, c=1). The calculation was performed using 8 cores to facilitate understanding of the figure, and the first two AMR iterations are reported. One can notice on this figure that the initial global numbering of mesh elements (performed by the Gmsh mesher [88]) has an influence on the mesh partitioning, both in the first and subsequent AMR iterations. Indeed, the global numbering of the mesh is used for initial partitioning and influences the new local numbering of the elements, obtained once the mesh partitioning is applied. Additionally, we should mention that, although the elements are staggered

among the MPI processes, the MFEM library handles this well internally. MFEM manages the lack of element cohesion through ghost elements, which are automatically added and tracked around elements within a given MPI process. These ghost zones act as internal boundaries and are added to transparently handle MPI communications with neighboring MPI processes.

As mentioned earlier, this mesh partitioning method, which was set up to handle contact, ensures the contact terms to be built without inter-MPI process communications. On the other hand, the proposed mesh partitioning induces MPI regions composed of elements that are scattered throughout the mesh. This can be seen even better in Figure 9 which displays the MPI task numbers assigned to the elements of a 3D mesh used for a AMR-contact simulation (here, c=1). The calculation was performed using 32 cores to have an acceptable number of colors, and the mesh edges are not represented to better distinguish the color changes that means a change of MPI task between two neighboring elements.

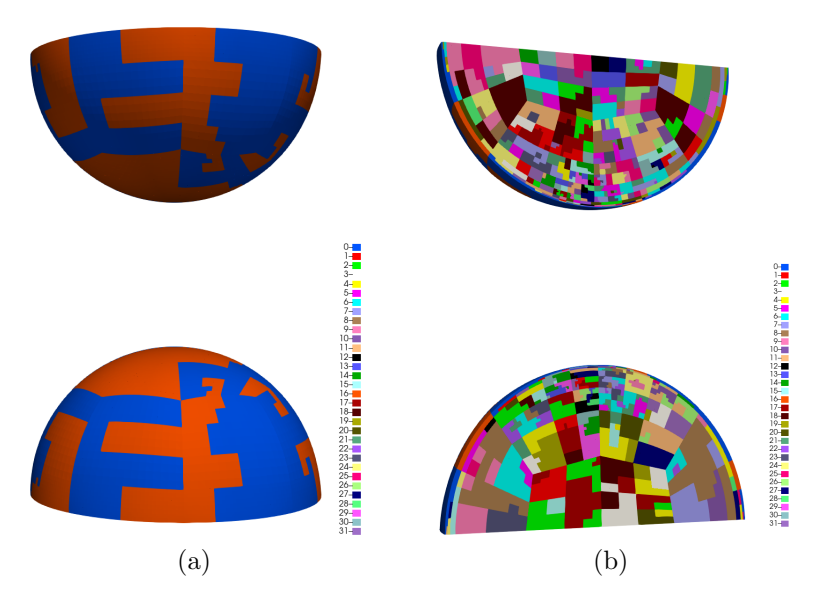


Figure 9: Contact-based load balancing illustration for a 3D mesh, typical of the Hertzian problem - Color representing the MPI task.

As expected contact paired nodes are on the same MPI task, but many MPI-task interfaces are created inside each solids.

#### 5. Application to the Hertzian contact problem

This section is devoted to illustrating the efficiency of the proposed parallel strategy and its suitability to contact mechanics problems with curved edges. To this end, academic Hertzian benchmark problems from [89] are considered is 2D and 3D. There are well-known reference test cases in contact mechanics, especially as analytical expressions of the stress field in the contact area are available to verify numerical strategy accuracy. The mechanical problem under consideration is defined by (1). The two 2D half-disks (resp. two 3D half-spheres) brought into contact are isotropic elastic materials with the same Young's modulus E=210 GPa and a Poisson's ratio  $\nu=0.3$ . Their radius is equal to R=2 m. Dirichlet boundary conditions of value  $u_D=\frac{\delta_0}{2}+\alpha R$ , where  $\delta_0=2$  m is the initial gap between solids and  $\alpha$  a positive coefficient, are imposed on the planar boundaries such as depicted for example in 2D in Figure 10.

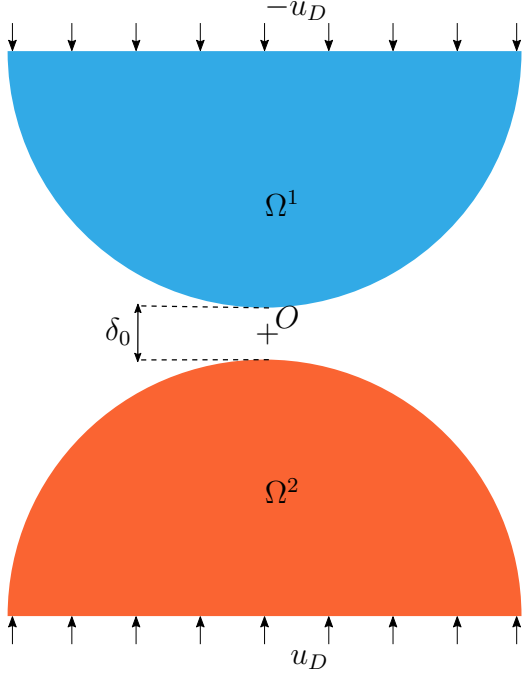


Figure 10: 2D Hertzian contact problem.

Two combinations of detection and stopping criteria for AMR are considered:

- AMR Combination 1: ZZ optimality criterion (15) and global stopping criterion (20);
- AMR Combination 2: LOC optimality criterion (16) and local stopping criterion (21).

The quantities of interest in our simulations are the relative global estimated error in energy norm  $\gamma_{\Omega} = \xi_{\Omega}/\omega_{\Omega}$ , the measure of the zone still marked for refinement at the end of the AMR process evaluated by the ratio  $\eta = \mu(\Omega_{\mathcal{M}})/\mu(\Omega^h)$ , the number of mesh elements  $N_E$  and the number of DOFs N. These quantities of interest make it possible to quantitatively compare the two considered AMR combinations.

# 5.1. Justification of the penalty parameter $k_N$

Although the penalty method is a classical and widespread method for numerical treatment of contact problems, see for example [14, 15, 2], the choice of an optimal penalty parameter (see  $k_N$  is Eq. (7)) remains the main limitation of this method. Indeed, the generated interpenetration error is directly related to the penalization parameter  $k_N$ , and goes to zero only in an asymptotic case, when  $k_N$  tends towards infinity. However, a too large penalty coefficient consistently produces ill-conditioning of the stiffness matrix  $\hat{\mathbf{K}}_C$ , leading to severe convergence issues in the solution of Problem (8).

To limit the value of the penalty coefficient while controlling interpenetration, it has been proposed in [90] to add a shift parameter to the penalty contribution, which is incrementally updated with the residuals obtained when solving the linear system with an iterative solver. This method results in dynamically shifting the point from which the penalty potential is applied to the problem toward the gap-open side, to reduce interpenetration due to contact without increasing the penalty parameter. This solution has not been adopted in our work, as it involves correcting the system to be solved during the solver's iterations, which is not possible when using black-box solvers such as those from the Hypre library, for example. On the other hand, a convergence analysis of the penalty method for 2D and 3D contact problems has been carried out in [91]. This study shows that the same mesh convergence rates with methods that directly solution the saddle-point problem arising from the contact formulation are obtained by choosing  $k_N$  inversely proportional to h (the mesh size).

Our proposal to choose the penalty coefficient is defined in two steps. The first step consists in comparing the results obtained with the penalty method with those obtained with Lagrange multiplier method. To do this, the contact forces (see  $\mathbf{L}^C$  in Problem (3)) derived from both methods are compared:

- $\mathbf{L}^{C}(\lambda) = \hat{\mathbf{B}}^{T} \lambda$ , for the Lagrange multiplier method, where  $\lambda$  denoted the Lagrange multiplier solution
- $\mathbf{L}^{C}(\mathbf{U}) = k_{N}\hat{\mathbf{B}}^{T}(\hat{\mathbf{D}} \hat{\mathbf{B}}\mathbf{U})$  for the penalty method

Lagrange multiplier contact forces are obtained thanks to simulations performed with the finite elements software Cast3M [92], developed by CEA (French Alternative Energies and Atomic Energy Commission), that is based on a Lagrange multiplier method for contact mechanics. Penalized contact forces are obtained with our penalized contact solver implemented in MFEM. It should be noticed that for all these comparisons, the input mesh used in Cast3M and MFEM, presented in Figure 11b, is identical. Thus, we consider a 2D conforming fine discretized  $Q_1$  (bilinear test functions) mesh with a mesh step of around  $h \simeq R/2^8 = 2^{-7}$  m, i.e. 200 thousands of nodes in total (100 thousands of nodes in each half-disk). This mesh is directly obtained in Gmsh mesher through 6 steps of uniform and isotropic refinement of an initial coarse mesh reported in Figure 11a. Hence, the refined mesh is geometry-fitted. Here, for the 2D meshes, the order of the super-parametric transformation is chosen equal to 10.

Figure 12 plots the contact forces obtained with our MFEM penalized contact algorithm for different values of the penalty parameter, from  $k_N = \text{E (N.m}^{-1})$  to  $k_N = 10^7 \cdot \text{E (N.m}^{-1})$  by steps of a factor of 10 (without modifying the input mesh), as well as the contact forces obtained using the Lagrange multiplier method, considered as the reference solution. Here,  $\alpha$  is equal to 0.15.

As expected, the penalized forces converges towards the Lagrange multiplier forces when the penalty parameter increases. Zooms made in Figures 12b and 12c clearly show a poor accuracy for  $k_N = \mathrm{E} \ (\mathrm{N.m^{-1}})$  and  $k_N = 10 \ \mathrm{E} \ (\mathrm{N.m^{-1}})$ . Thus, a penalty coefficient of at least  $10^2 \cdot \mathrm{E} \ (\mathrm{N.m^{-1}})$  is required. In addition, the choice  $k_N = 1 \cdot \frac{\mathrm{E}}{h} = 128 \cdot \mathrm{E} \ (\mathrm{N.m^{-1}})$  derived from [91], is perfectly in line with this conclusion and might be suitable.

In addition, Figure 13 illustrates the influence of the mesh step and the penalty coefficient on the interpenetration of contact surfaces for two

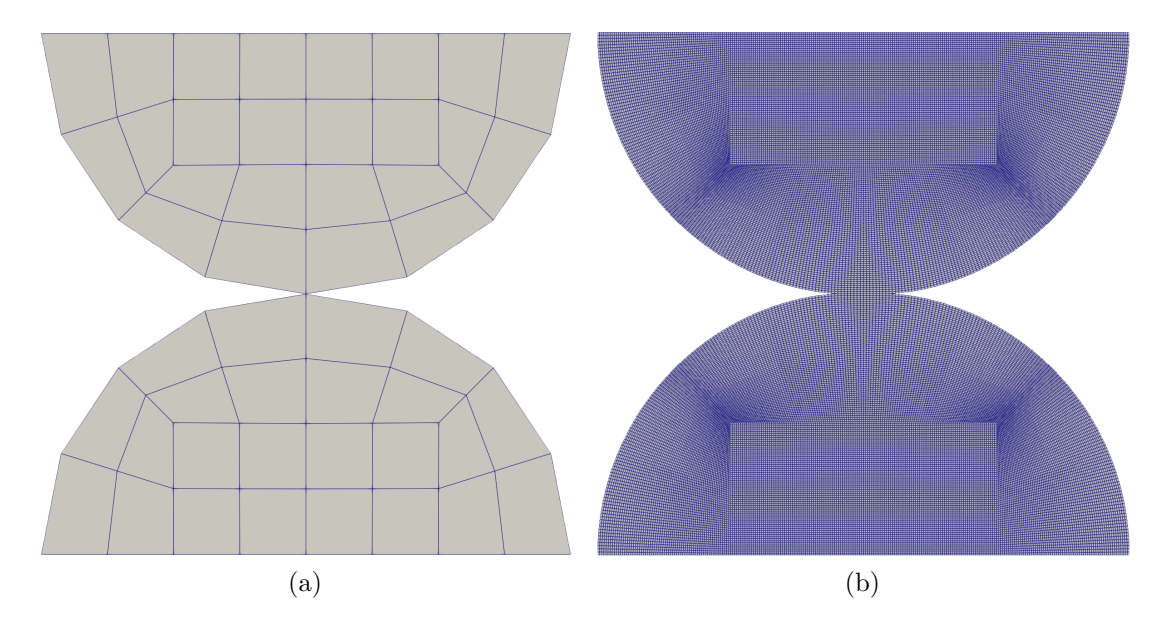


Figure 11: 2D Hertzian contact problem: initial in (a), and fine in (b) quadrilateral meshes

uniformly refined meshes, refined 6 (in blue) and 7 (in orange) times from the same initial mesh (with a mesh step of  $h_{ini}$ ). On the one hand, this figure confirms that, for the same finite element simulation, increasing the penalty coefficient logically tends to decrease the interpenetration of the surfaces. On the other hand, this figure allows us to observe that, for the same penalty coefficient, the ratio of interpenetration to mesh step remains constant for the two different meshes. This suggests that increasing the penalty coefficient is not the only solution to reduce interpenetration. Indeed, decreasing the mesh step leads, for a fixed penalty coefficient, to improve the accuracy of the solution. This result can be justified by the fact that the more nodes there are on the contact boundaries, the lower the nodal value of the contact force on each of these nodes, and the lower the interpenetration resulting from the same penalty. Thus, choosing a constant penalty coefficient during the AMR iterations means reducing the interpenetration with the mesh step.

The second step consists in comparing strategies for setting  $k_N$  during a 3D AMR simulation with respect to several quantities of interest: the number of elements  $N_E$  and degrees of freedom (DOFs) N, the total and solver times,  $T_{tot}$  and  $T_{solver}$  respectively. Here, AMR Combination 1 with

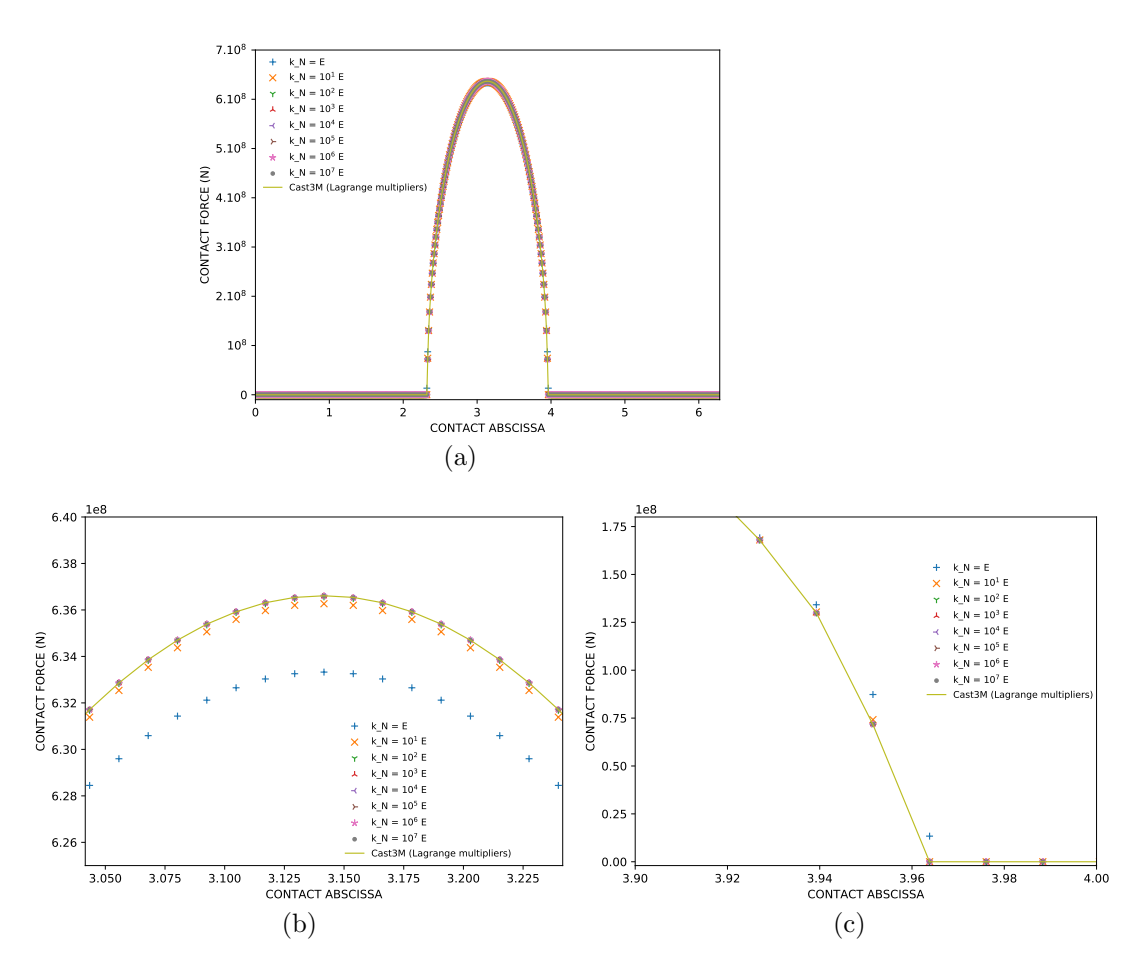


Figure 12: Contact force distribution over the potential contact zone (half-disks of Hertz). General overview in (a). Zoom on the contact center zone in (b) and on the contact status change area in (c).

 $e_{\Omega}=2\%$  is considered. The initial mesh is built in the Gmsh mesher from the mesh shown in Figure 5a (in cross-section view), to which a uniform level of refinement has been applied (by the mesher). The resulting mesh, presented in Figure 14a (in cross-section view), contains 2484 nodes and 2048 finite elements and is fitted to the contact curve boundaries. Here, for the 3D meshes, the order of the super-parametric transformation is chosen equal to 6. The final mesh obtained is shown in Figure 14b. Note that here, as for the sequel,  $\alpha$  is equal to 0.015. Let us underline that the revolution asymmetry of the resulting refined mesh with respect to the vertical axis is a direct consequence of the initial mesh that does not respect a revolution

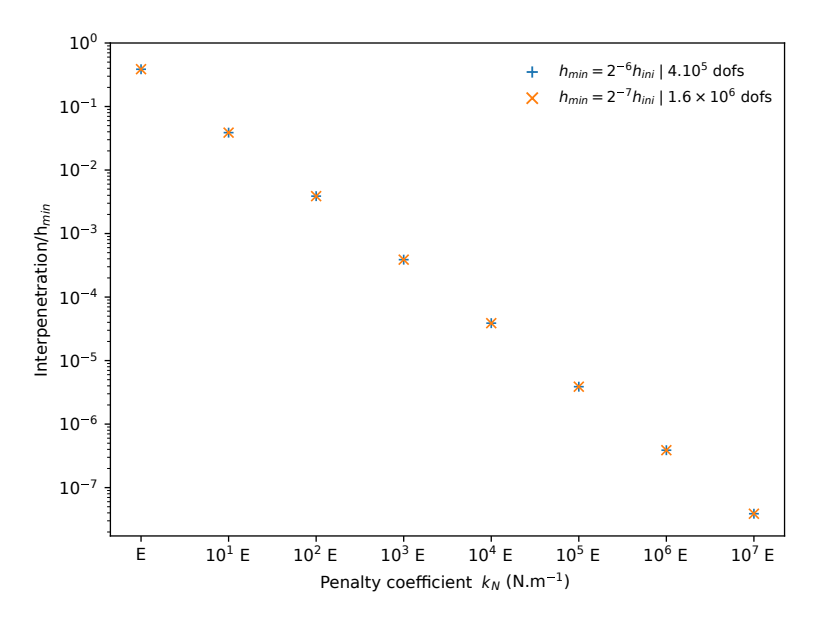


Figure 13: 2D Hertzian contact problem : influence of  $k_N$  and mesh step  $h_{min}$  on the interpenetration of the surfaces.

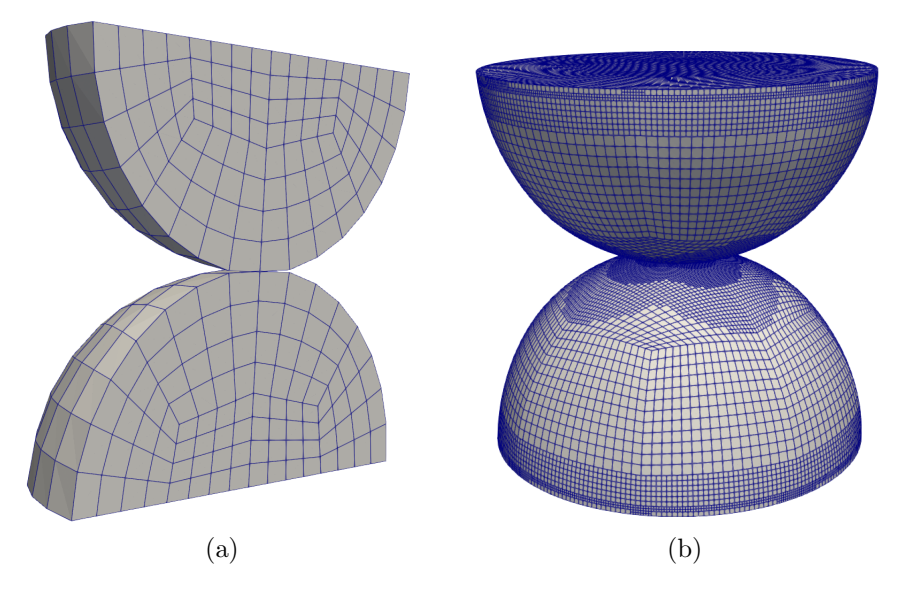


Figure 14: 3D Hertzian contact problem: (a) cross-sectional view of the initial mesh, (b) final mesh for AMR Combination 1 with  $e_{\Omega}=2\%$  and  $k_N=10^2$  E (N.m<sup>-1</sup>) - 6th-order transformation.

symmetry around this axis.

Simulations were performed on four calculation nodes of the CCRT/CEA Topaze supercomputer (AMD Milan processors) each hosting 128 cores per node, so 512 cores in all. Table 1 summarizes some results obtained for the different choices of  $k_N$ . The last choice correspond an adaptation to nodal contact forces with AMR of the suggestion of [91] where  $k_N$  depends on  $h_{\min}$ , the minimum discretization size of the current AMR iteration. This results in increasing  $k_N$  during the AMR iterations, which implies even greater solution accuracy (lower interpenetration) for refined meshes. Let us underline that keeping  $k_N$  constant during AMR iterations already results in reducing the interpenetration as the mesh step decreases (since the values of the nodal forces also decrease).

$k_N  (\mathrm{N.m^{-1}})$	$N_E$	N	$T_{tot}$ (s)	$T_{solver}$ (s)
E	$7.85 \times 10^{5}$	$1.377 \times 10^7$	452	311
10 E	$7.84 \times 10^{5}$	$1.375 \times 10^{7}$	426	308
$10^{2} {\rm E}$	-	-	427	309
$10^{3} {\rm E}$	-	-	436	304
$10^4 { m E}$	-	-	445	305
$10^{5} {\rm E}$	-	-	441	306
$10^{6} {\rm E}$	-	-	426	307
$10^7 \mathrm{E}$	-	-	437	303
$rac{\mathrm{E}}{h_{\mathrm{min}}}$	-	-	431	306

Table 1: Influence of the penalty parameter  $k_N$  on the AMR simulation with a target global error  $e_{\Omega}=2\%$  - Average times over 3 calculations - The '-' symbol indicates that the value is identical to the last entry in the column.

All simulations ended after 5 refinement steps, so that the final mesh step  $h_{fin}$  is around  $2^{-5}h_{ini}$  with  $h_{ini}$  the initial mesh step. For  $k_N$  greater than  $10 \cdot \mathrm{E} \ (\mathrm{N.m^{-1}})$ , the results in terms of AMR are similar. In addition, the computation times vary only slightly with the chosen penalty coefficient. Indeed, variations of around 6 % are observed for the total computation time, and not exceeding 3 % for the solver time. Thus, the results tend not to depend too much on the penalty coefficient as soon as this latter is superior or equal to 10 E  $(\mathrm{N.m^{-1}})$ . By choosing a variable penalty

parameter as defined in Table 1 (last row), it is observed that  $k_N$  exceeds 10 E (N.m<sup>-1</sup>) starting from the fourth AMR iteration and seems also suitable.

From this two studies, it was decided to set the penalty coefficient to be constant at  $k_N = 10^4 \cdot \text{E (N.m}^{-1})$  to achieve a satisfactory compromise between surface interpenetration and simulation convergence, even for small elements. Indeed, choosing  $k_N = 10^4 \cdot \text{E (N.m}^{-1})$  does not seem any more costly in terms of calculation time than  $k_N = 10^2 \cdot \text{E (N.m}^{-1})$ , and reduces interpenetration even further. Increasing the penalty coefficient with the mesh step is not required here as the penalization directly affects the nodal forces.

## 5.2. Comparison with Hertz analytical solution

To assess the accuracy of the proposed solution strategy, it is relevant to compare the results obtained with those derived from the Hertz's theory (see [89] for further details). To stick to the scope of Hertz's theory, the following conditions must be satisfied:

- solids have elastic, homogeneous and isotropic mechanical behaviour;
- the infinitesimal strain theory is applied;
- the contact surfaces are small compared to the whole solids and the deformations outside these surfaces are negligible compared to those on them;
- no contact friction.

Thus, for this analysis, the 2D test case is under consideration and the fixed Dirichlet boundary conditions  $(u_D - \frac{\delta_0}{2} = 0.015 \, R)$  respect the criteria of the infinitesimal strain theory. In addition, we still rely on the Combination 1 for the AMR process.

Hertz's theory defines the following contact pressure distribution:

$$p(r) = p_{\rm O}\sqrt{a^2 - r^2}/a \; ; \; r \le a$$
 (35)

where a is the characteristic contact distance, r the (positive) distance from the center O of the contact zone, and  $p_{\rm O} = p({\rm O})$  the maximum contact pressure at center O. To calibrate the Hertz solution for our test case, a

highly refined mesh has been used to perform a reference solution, which yields a=0.199 and  $p_{\rm O}=11.5$  GPa. These values are then used to define the Hertz pressure distribution, which is compared in Figure 15 with the contact pressures obtained via the finite element solution  $p=-\sigma_C=-(\boldsymbol{\sigma}\mathbf{n})\cdot\mathbf{n}$  on  $\Gamma_C$ . In this Figure, the origin of the contact abscissa is chosen as the center O of the contact zone. The results clearly show that by decreasing the user-specified accuracy  $e_{\Omega}$  for the AMR application, the finite element solution is refined in the contact area and tends towards the closed-form expression derived from Hertz theory. Moreover, this example shows the efficiency of the super-parametric transformation to capture the curved boundary during the hierarchical AMR iterations.

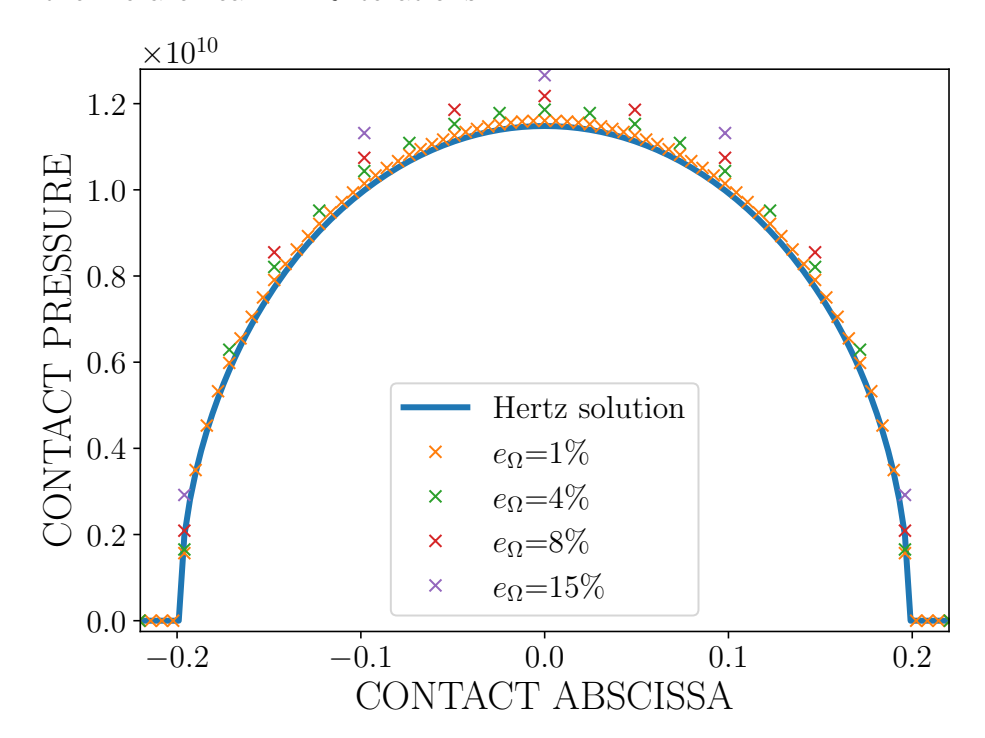


Figure 15: Contact pressure distribution over the contact zone (half-disks of Hertz).

#### 5.3. On the AMR strategies

In order to assess the interest of performing AMR instead of uniform refinement, convergence in mesh-step and in number of nodes is performed for the 2D case. To this end, a reference solution (on the whole surface) is performed on a very fine discretized mesh of linear finite elements with a

mesh step of around  $R/2^{10}$ , i.e. 3.2 million nodes in all (1.6 million nodes for each half-disk). For this mesh convergence study, linear or quadratic isoparametric finite elements are considered. Indeed, as mentioned in [93] and the references cited therein, the contact solution is at best in the Hilbert space  $H^{5/2}$ . Hence, only finite element methods of order one and of order two are really of interest. To evaluate the approximation error on the computational domain, uniformly isotropically pre-refined (by the Gmsh mesher) meshes are used. An example of an initial mesh with first-order elements is given in Figure 11a. In its turn, the AMR method is applied on linear finite elements only. In addition, as mesh convergence studies involves global errors (on the whole domain), AMR Combination 1 is considered here. Figure 16 shows the mesh convergence of uniformly refined solutions as well as the convergence in mesh nodes for uniformly and locally (with AMR) refined solutions.

On the one hand, it is observed that the uniformly refined solutions respect the convergence rates predicted by finite element theory in the presence of contact between two solids, see [94, 93] for example. For the energy norm, these convergence rates are in  $\mathcal{O}\left(h^{\min(k,\tau-1)}\right)$  according to the mesh size and in  $\mathcal{O}\left(N^{-\min(k/m,(\tau-1)/m)}\right)$  with respect to the number of DOFs (directly proportional to the number of mesh nodes). In these formula, k denotes the degree of interpolation of the basis functions,  $\tau$  the regularity of the solution (here  $\tau = 5/2$ ), and m the dimension of the space. Hence, for contact problems solved by finite elements of order greater than 1, sub-optimal convergence rates (here in 3/2) are obtained, see Figure 16a.

On the other hand, first-order solutions obtained with AMR exhibit better convergence rates in DOFs than solutions obtained with a uniformly refined mesh, see Figure 16b. A superconvergence of the first-order AMR solutions is observed, as they perform as well as uniformly refined second-order solutions. As expected, AMR errors are smaller than for uniformly refined first-order solutions for a given number of DOFs. Moreover, the number of DOFs is at least approximately 10 times smaller for the AMR solution for a given error producing sufficiently accurate solutions. This substantial gain justifies the interest in implementing an AMR strategy.

The ESTIMATE-MARK-REFINE approach considered in our study, combining quantitative detection and stopping criteria, has recently proven its efficiency in a solid mechanics context [73] but without contact. Thus, the enrichment of the currently implemented h-adaptive method in MFEM

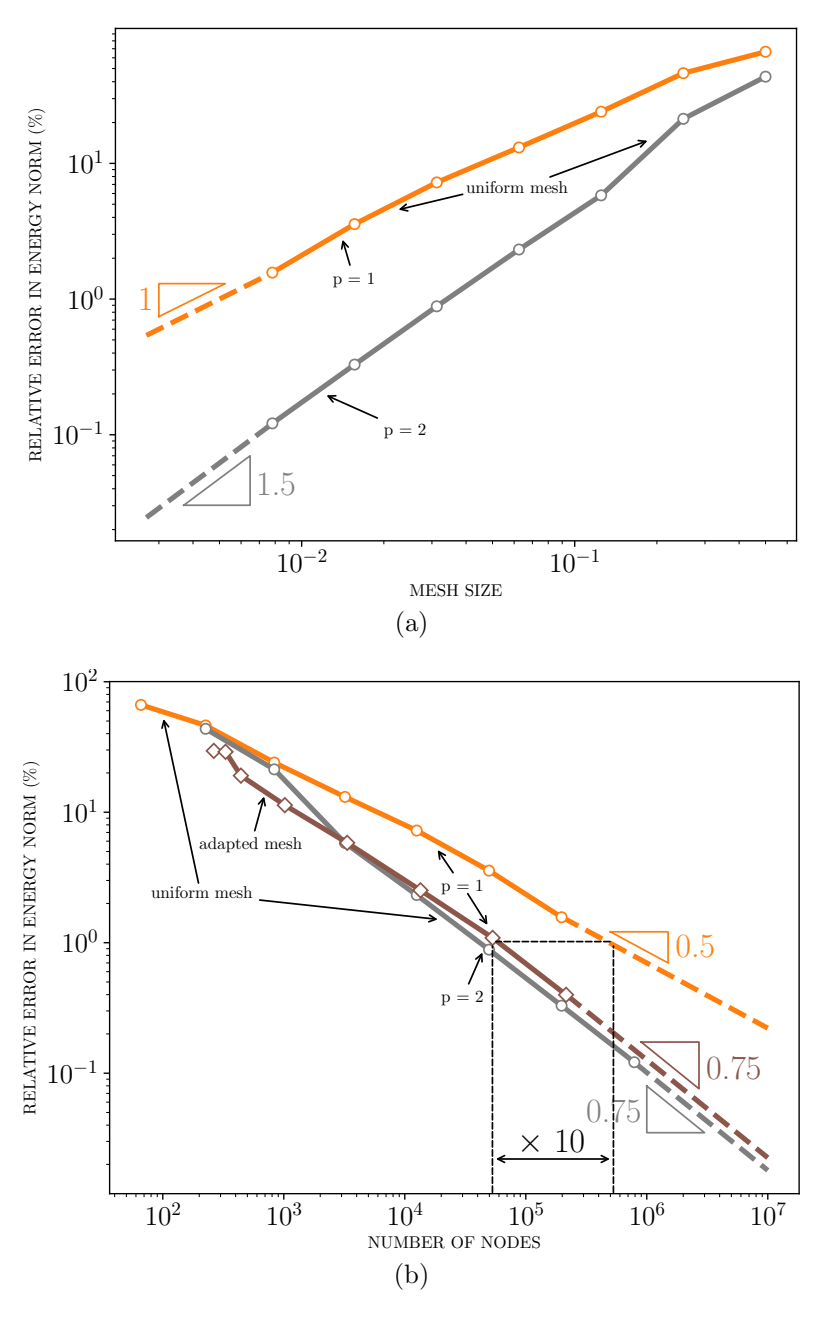


Figure 16: Discretization errors (half-disks of Hertz) with respect to the mesh size and to number of nodes for uniform refinement and AMR approaches.

with this strategy is evaluated on the Hertzian contact problem hereafter. For this case study, the 3D half-spheres are brought into contact and the two AMR combinations introduced above are considered.

**Remarks:** Since a very fine, uniformly refined 3D mesh is very costly in terms of computation time and memory footprint, error results are not compared here to a reference solution. The initial mesh for calculations (performed here with 512 MPI processes) is shown in Figure 14a.

Table 2 details the results obtained with AMR Combination 1 for different values of  $e_{\Omega}$  from 2% to 1% while Figure 17 shows the refined mesh obtained for  $e_{\Omega} = 2\%$ .

				Number of
	$\gamma_\Omega(\%)$	$\eta(\%)$	$N_E$	refinement steps
$e_{\Omega} = 2\%$	1.84	15.4	$7.84 \times 10^{5}$	5
$e_{\Omega} = 1.7\%$	1.14	29.9	$2.41 \times 10^{6}$	6
$e_{\Omega} = 1.5\%$	1.08	33.0	$3.07 \times 10^{6}$	6
$e_{\Omega} = 1.2\%$	0.976	21.2	$4.59 \times 10^{6}$	7
$e_{\Omega} = 1\%$	0.925	16.1	$6.27 \times 10^{6}$	7

Table 2: 3D Hertzian contact - AMR Combination 1 - results in errors and number of AMR iterations

Similarly, Table 3 provides the results obtained with AMR Combination 2 for  $e_{\Omega, \text{LOC}} = 7\%$  to 2% and  $\delta = 0.1\%$ , while Figure 18 displays the refined mesh obtained for  $e_{\Omega, \text{LOC}} = 7\%$  and  $\delta = 0.1\%$ . Here,  $e_{\Omega, \text{LOC}}$  is globally chosen to be greater than  $e_{\Omega}$  because AMR Combination 2 tends to locally more refine than AMR Combination 1, see Tables 2 and 3 for the error value of 2% for example.

First of all, we observe that for AMR Combination 1 (see Figure 17), mesh refinement is spread in the contact area, whereas for AMR Combination 2, Figure 18 shows that the finest edges (corresponding to the highest level of refinement) are located in the zone where the contact status (contact/no contact) changes, which is in coherence with the results obtained in [31] with the same LOC optimality criterion. Both tables show that, whatever the selected combination, the user-prescribed error threshold  $e_{\Omega}$  (resp.  $e_{\Omega,LOC}$ ) is respected, i.e.  $\gamma_{\Omega} < e_{\Omega}$  (resp.  $\gamma_{\Omega} < e_{\Omega,LOC}$ ), especially for AMR Combination 2 where this condition is not imposed. In addition, for an equivalent relative

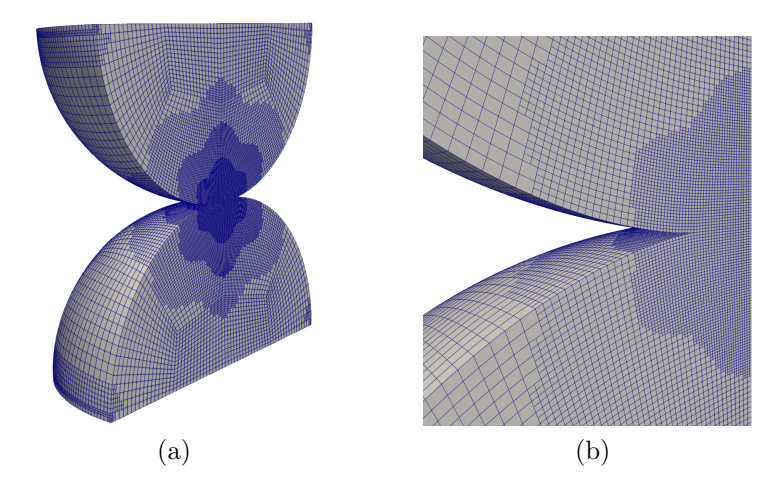


Figure 17: 3D Hertzian contact - AMR Combination 1 ( $e_{\Omega} = 2\%$ ). Cross sectional view in (a) - and zoom around the contact center zone in (b) - 6th-order transformation.

				Number of
	$\gamma_{\Omega}(\%)$	$\eta(\%)$	$N_E$	refinement steps
$e_{\Omega, LOC} = 7\%, \ \delta = 0.1\%$	5.11	0.0537	$2.88 \times 10^{5}$	5
$e_{\Omega, LOC} = 5\%, \ \delta = 0.1\%$	3.60	0.0182	$1.05 \times 10^{6}$	6
$e_{\Omega, LOC} = 4\%, \ \delta = 0.1\%$	2.92	0.0330	$1.73 \times 10^{6}$	6
$e_{\Omega, LOC} = 3\%, \ \delta = 0.1\%$	2.21	0.0108	$4.64 \times 10^{6}$	7
$e_{\Omega, \text{LOC}} = 2\%, \ \delta = 0.1\%$	1.47	0.0363	$1.34 \times 10^{7}$	7

Table 3: 3D Hertzian contact - AMR Combination 2 - results in errors and number of AMR iterations

global error  $\gamma_{\Omega}$ , the mesh obtained contains fewer elements when using AMR Combination 1, but the use of this combination does not effectively control the zone where the local prescribed error is not respected, see  $\eta$  in row 1 of Table 2 versus in row 5 of Table 3. On the contrary, choosing AMR Combination 2 to apply AMR enables us to more efficiently characterize the critical regions, see Figure 20 versus Figure 19, where the number of AMR iterations is the same. The

Thus, the choice of the relevant combination of AMR criteria depends on what is of interest to control. On the one hand, if the main aim is to control the global error only, then choosing Combination 1 enables to obtain an acceptable mesh with less DOFs. On the other hand, if our priority is to

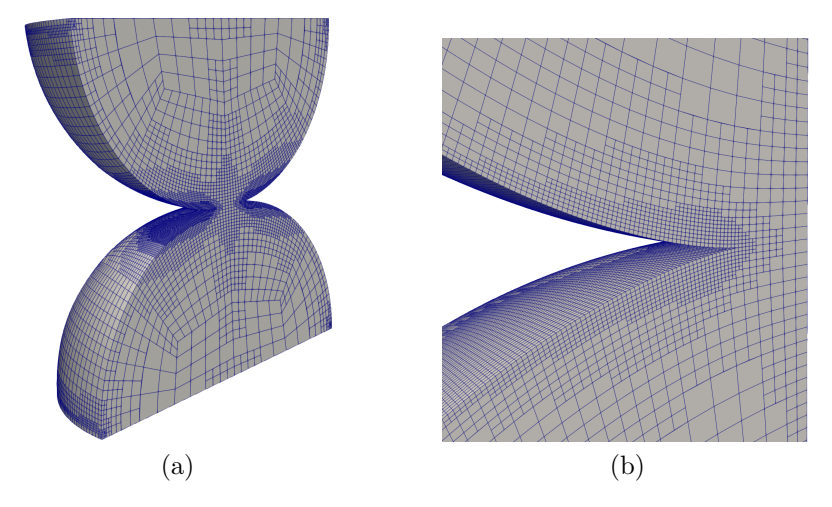


Figure 18: 3D Hertzian contact - AMR Combination 2 ( $e_{\Omega,LOC} = 7\%$ ,  $\delta = 0,1\%$ ). Cross sectional view in (a) and zoom on the contact center zone in (b) - 6th-order transformation.

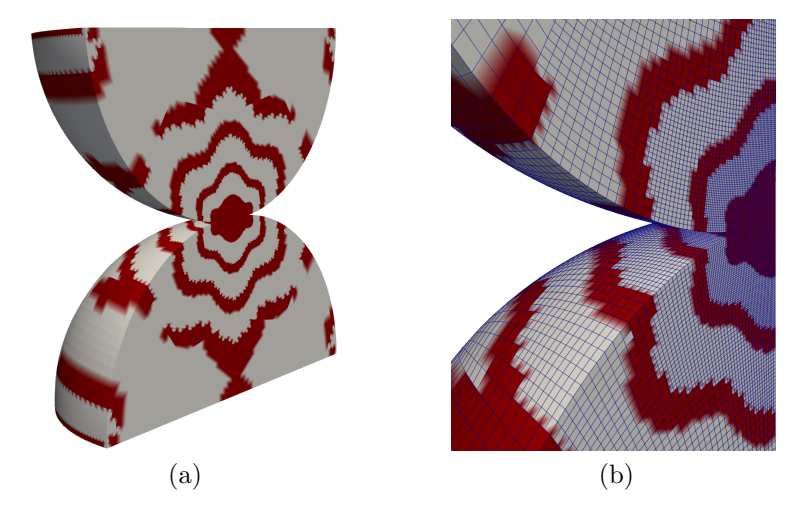


Figure 19: 3D Hertzian contact - AMR Combination 1 ( $e_{\Omega} = 2\%$ ). Zones still marked for refinement at the end of the AMR process in red. Cross sectional view in (a). Zoom on the contact center zone in (b) - 6th-order transformation.

locally handle the error, then choosing Combination 2 is required.

The Figures 17 to 20 show that the symmetrical nature of the problem (identical geometries, same materials) results in perfectly identical refinement of the two solids, where the nodes are strictly facing each other. However, as previously mentioned the initial mesh induces a revolution

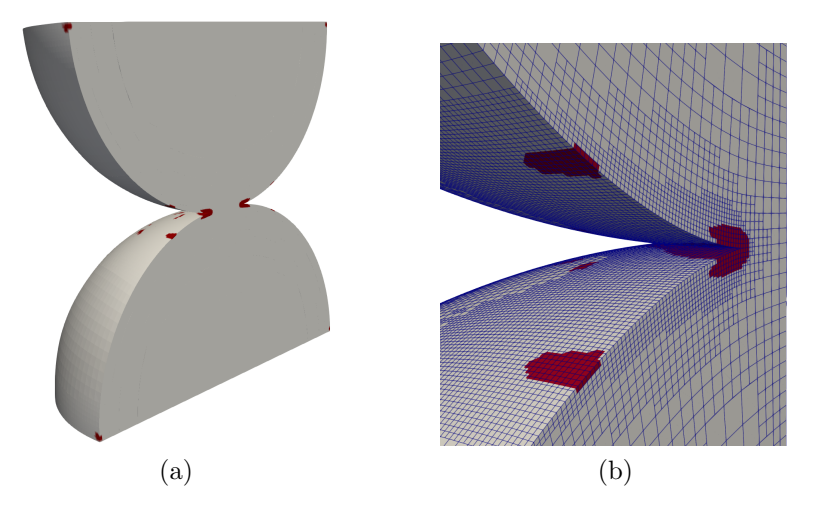


Figure 20: 3D Hertzian contact - AMR Combination 2 ( $e_{\Omega,LOC} = 7\%$ ,  $\delta = 0, 1\%$ ). Zones still marked for refinement at the end of the AMR process in red. Zoom on the contact center zone in (b) - 6th-order transformation.

asymmetry around the vertical axis of all the refined meshes.

We are also interested in verifying the effectiveness of the AMR strategy employed in the case of contact between two solids with different mechanical properties. Simulations were performed with two solids presenting a contrast of  $10^4$  in Young's modulus (the Poisson ratio remains the same). The lower solid is then more rigid than the upper one, which keeps the material characteristic previously considered ( $E_1 = 210 \text{ GPa}$ ). The same Dirichlet boundary conditions than those introduced at the beginning of the section were applied and AMR Combination 1 was chosen. An example of the results obtained is reported in Figure 21. Several observations are worth noting. Firstly, the AMR process is applied distinctly between solids in contact, and it can be seen that the most deformable solid is the most refined overall. Moreover, the mesh solution obtained shows the effect of the detection enlargement criterion (18), as all potential contact paired elements are refined in the same way.

### 5.4. Parallel scalability

To demonstrate the parallel scalability of our method, we have carried out numerical studies with a varying number of cores for representative simulations of the 3D half-spheres Hertzian contact problem.

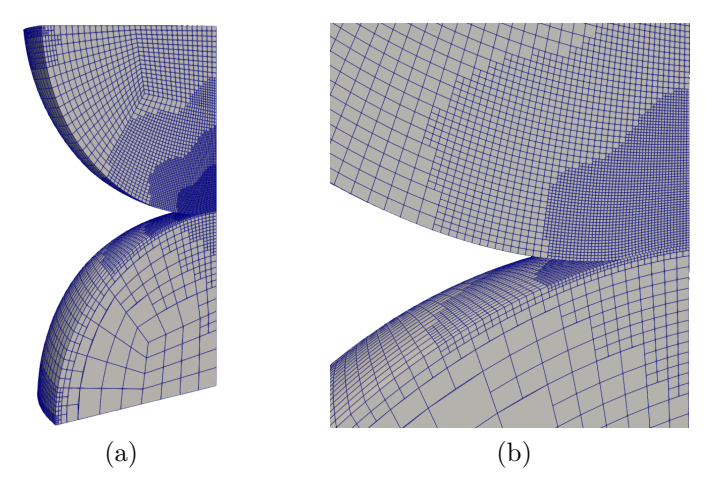


Figure 21: 3D Hertzian contact between different materials - AMR Combination 1 ( $e_{\Omega} = 2\%$ ). Cross sectional view in (a) and zoom on the contact center zone in (b) - 6th-order transformation.

In addition to the total calculation time, the times of the following main program functions are monitored:

- assembling the finite element stiffness matrix (mfem::ParBilinearForm::Assemble MFEM function);
- forming the linear system (mfem::ParBilinearForm::FormLinearSystem MFEM function, equation (28));
- solving the matrix system (apply the solver from mfem::PenaltyPCGSolver MFEM class, equation (8));
- refining elements (ESTIMATE-MARK-REFINE AMR approach, mfem::MeshOperator::Apply MFEM function);
- load balancing the whole mesh after refinement (including the mfem::ParNCMesh::Rebalance MFEM function).

First of all, AMR Combination 1 is applied to the benchmark. The threshold  $e_{\Omega}$  is set to 2% and the resulting mesh has been already shown in the previous section, see Figure 17. This mesh is obtained after 5 refinement steps and the discrete solution **U** to be solved is of size  $2.3 \times 10^6$  (number of conforming DOFs).

To set the coefficient c in the load balancing formula (33), calculations are performed by varying this coefficient for a constant number of MPI tasks. The results obtained are presented in Figure 22 for 512 MPI tasks, and show that setting this parameter to 1 seems to be an optimal choice. Furthermore, since in our strategy MFEM distributes calculations according to the specified partition of elements, these results demonstrate that balanced partitioning of the mesh is essential in optimizing the algorithm's performance. Other calculations not presented here have shown that choosing a different number of MPI processes produces time measurements leading to the same conclusion for the choice of c.

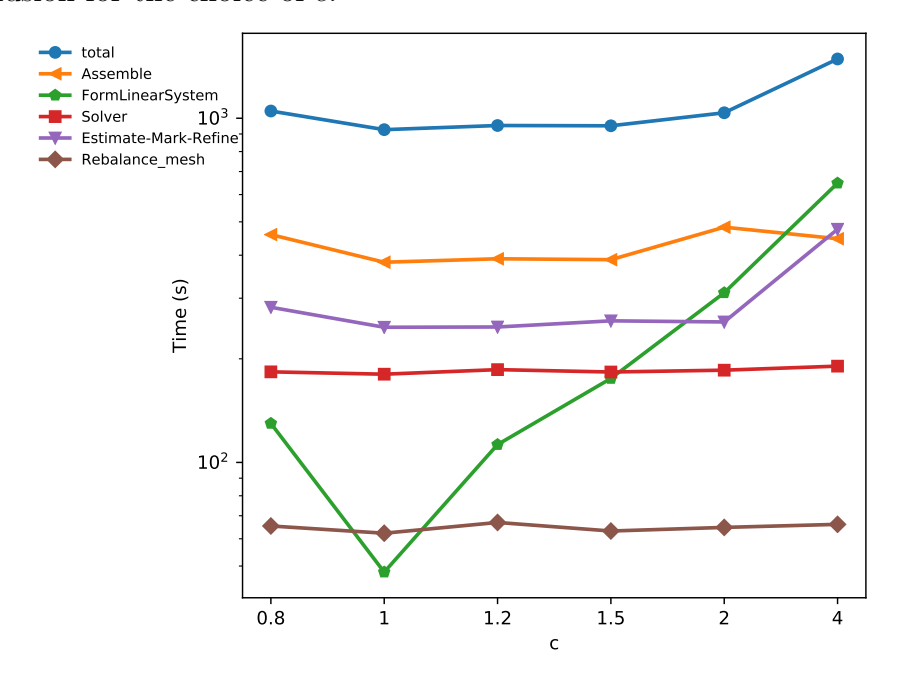


Figure 22: Computation times, scan for different values of c - 3D Hertzian contact - AMR Combination 1 ( $e_{\Omega} = 2\%$ ).

It is of interest to study the parallel performance of our strategy on larger meshes. This is why, in the scalability analysis reported in Figures 23 and 24, the contact problem is solved by applying AMR Combination 1 with  $e_{\Omega} = 1.5\%$ , and AMR Combination 2 with  $e_{\Omega,LOC} = 4\%$  and  $\delta = 0.1\%$ . The resulting solutions are obtained after 6 refinement steps and the discrete solution **U** of the last 'conforming' problem is of size  $9.0 \times 10^6$  and  $5.1 \times 10^6$  respectively. Calculations were performed on the calculation nodes of the CCRT/CEA Topaze supercomputer (AMD Milan processors) each hosting

128 cores per node. The initial uniformly refined mesh is designed so that there are always more elements than the maximal number of parallel tasks for the study. The following results are obtained solving the conforming linear system using Hypre's conjugate gradient solver (HyprePCG), preconditioned by the incomplete LU factorization strategy available in Hypre (HypreILU).

During the simulations, it has been observed that the memory footprint of the calculations was high (mainly due to the distributed mesh management within MFEM and constitutes our main limiting factor. Thus, in order to carry out our strong scaling studies, it has been decided to allocate 4 cores to each processor used. Table 4 reports the memory footprint used for AMR Combination 1 with  $e_{\Omega}=1.5\%$  for 256, 512 and 1024 cores. This memory footprint is listed for calculations using Hypre's ILU preconditioner but also BoomerAMG preconditioner as well as without any preconditioner. For each simulation, the percentage of the total memory footprint used is given for the following steps:

- the last refinement step;
- the last load rebalancing step;
- the steps for solving the matrix system during the last AMR iteration.

Preconditioner	Ø			HypreBoo	HypreILU			
CPU cores	256	512	1024	256	512	256	512	1024
Total memory footprint (GB)	662	973	1545	875	1218	671	977	1546
Last refinement step (%)	40.4	34.5	28.2	22.4	21.9	40.7	34.9	28.3
Last rebalance step (%)	8.2	11.0	18.8	6.3	8.6	8.1	10.9	18.8
Last AMR iteration - Solver steps (%)	0	0	0	20.5	17.0	0	0	0

Table 4: Memory footprint - 3D Hertzian contact - AMR Combination 1 ( $e_{\Omega} = 1.5\%$ )-HyprePCG solver with different preconditioner - number of final mesh conforming DOFs:  $9.0 \times 10^6$  - 6th-order transformation

Note that the simulation for 1024 cores with HypreBoomerAMG preconditioner did not converge, for a reason that will be explained later. The

increase in memory consumption as a function of the number of cores is due to the duplication of data structures required for the ghost layers. Table 4 shows that, as expected due to the increasing number of DOFs, the last refinement step consumes a lot of memory space. The last load rebalancing step is also a major memory space consumer, but less than the last refinement step. Finally, the last solutions of the matrix system induce a large cost in terms of memory space when the system is solved with a HypreBoomerAMG preconditioning but not at all with HypreILU or without preconditioner. This cost in memory space for the solver step with HypreBoomerAMG preconditioning is due to the storage of the preconditioning matrix, which is much larger than for HypreILU preconditioning. Indeed, during the solver steps of the last AMR iteration, the number of non-zero coefficients in the preconditioning matrix is about 2 times higher with HypreBoomerAMG than with HypreILU as preconditioner for the calculation using 256 cores, and is 4 times higher for the calculation using 512 cores. When measuring memory, it was observed with HypreBoomerAMG that the memory footprint is larger than the memory footprint due to the theoretical storage of the preconditioning matrix resulting from the number of non-zero coefficients found in Hypre. This could be due to the parallelism of the preconditioning matrix.

Finally, for large 3D calculations and with the aim of reducing computational costs (computation time and memory footprint), a solution could be to reduce the order of the super-parametric transformation or even to implement a the super-parametric transformation solely on the contact boundaries. Nevertheless, this is appropriate for boundaries with curvature that does not vary significantly.

On the basis of preliminary calculations, we found for the 3D Hertzian test case that switching from a 6th order to a 3rd order (volume) transformation not only reduces the memory footprint allocated during calculation by a factor of 2, but also divides calculation times by a factor of 5.

For AMR Combination 1, Figure 23 displays the speedup in strong scaling, the total time and the individual algorithm steps times.

Comparing the results obtained with the ideal strong scaling result, where parallelization would be perfect and would not generate any overhead, we can observe that the scalability of the algorithm obtained is satisfactory, particularly up to 512 cores. On the other hand, a loss of performance is observed regarding the linear system solving step. The problem has been investigated with the Scalasca profiling tool [95]. The loss of scalability is due to unbalanced communication schemes and large communication volumes caused

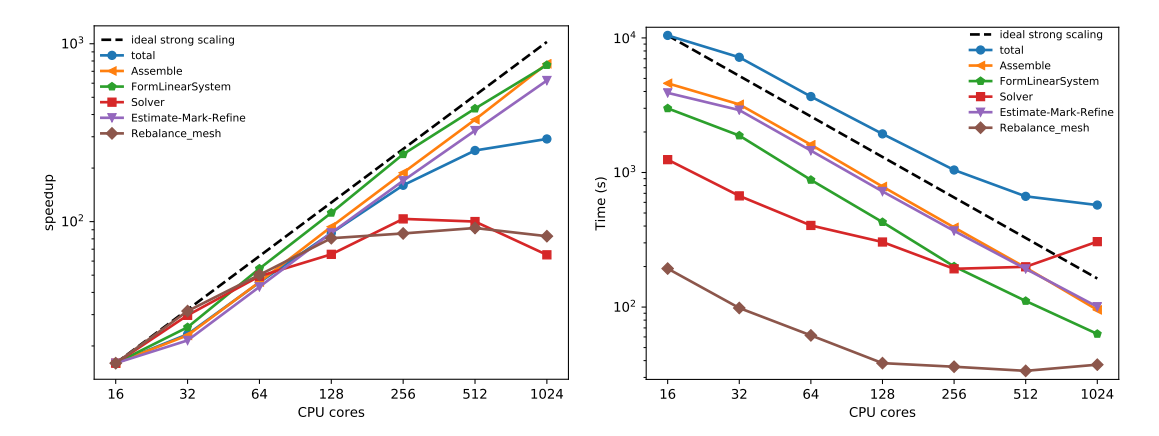


Figure 23: Performance results of the contact-AMR-HPC algorithm and its main steps - 3D Hertzian contact - AMR Combination 1 ( $e_{\Omega} = 1.5\%$ ) - HyprePCG solver with HypreILU preconditioner - number of final mesh conforming DOFs:  $9.0 \times 10^6$ .

by the mesh partitioning. The reason for this is that the set of elements owned by each process is composed of elements scattered throughout the mesh. This leads to large borders between parallel regions, and therefore extra communication costs. An in-depth profiling study has shown that the volume of communication is twice as high as calculations volume. The most costly operations are the MPI\_Allreduce() and MPI\_Waitall() reduction and communication operations, which take up almost 70% of the time spent in the solver. So, while the contact-aware partitioning reduces communication during contact evaluation, it leads to fragmented MPI domains with large interfacial regions, contributing to increased communication overhead during the solver phase. This topic is beyond the scope of this paper and will be addressed in future work, but we can shed some light on the subjects we're planning to investigate to reduce this overhead. An avenue for future research is to divide the finite element mesh into larger contiguous parts within each MPI process. This issue will be addressed with geometric partitioning techniques to split the mesh elements according to their spatial distribution. This kind of partitioning is generally quite cheap in term of execution time compared to graph-based approaches. In this regard, we are currently working on a solution that uses the Space Filling Curve (SFC) algorithm to generate a mesh partition and create large, parallel regions composed of closely grouped elements while ensuring contact paired elements to be on the same process.

A comparative study of solver performances regarding the choice of preconditioner is presented in Table 5. This table shows the number of iterations and execution times spent in the linear system solution step for two peculiar solving steps: the last (contact problem) solving step for the last two AMR iterations. These results are reported for 256, 512 and 1024 CPU cores for HypreBoomerAMG and HypreILU preconditioning, as well as without preconditioner.

Preconditioner		Ø			HypreBoomerAMG			HypreILU		
CPU cores		256	512	1024	256	512	1024	256	512	1024
Total - Solver										
steps	Time (s)	205.9	242.7	504.2	264.4	341.5	Ø	192.4	199.2	306.4
Second to last AMR iteration -	Number of itera- tions for PCG	2580	2571	2352	36	36	42	890	974	1039
Last solver step	Time (s)	16.0	27.2	58.1	29.6	37.9	44.2	13.8	20.6	22.4
Last AMR iteration -	Number of itera- tions for PCG	4487	3815	3810	38	37	Ø	1038	1059	1253
Last solver step	Time (s)	61.4	49.3	111.6	57.6	72.0	Ø	39.2	29.8	67.1

Table 5: Solving times - 3D Hertzian contact - AMR Combination 1 ( $e_{\Omega} = 1.5\%$ ) and HyprePCG solver with different preconditioners - number of final mesh conforming DOFs:  $9.0 \times 10^6$  - 6th-order transformation

As said before, the simulation with HypreBoomerAMG preconditioner fails to converge with 1024 cores. This is due to a non-symmetric-positive-definite (non SPD) preconditioning matrix issue. This type of problem was also encountered by modifying the set of parameters of the study case, for example by using AMR Combination 2 or by changing the value of the penalty coefficient. Modifying the Strong Threshold, the HypreBoomerAMG parameter defined as the most important option by MOOSE platform developers [96], does not enable us to tackle this issue. Since using the conjugate gradient solver developed in MFEM leads to exactly the same issue, it seems that the problem comes from the association of this preconditioner with a conjugate gradient solver, but not from the solver itself. In addition, simu-

lations with HypreILU as a preconditioner or without a preconditioner are going well. During our studies, we observed that using solvers that don't require a symmetric-positive-definite (SPD) preconditioning matrix, such as GMRES or BiCGSTAB, allows you to get round this HyperBoomerAMG issue, at the cost of larger computational time. Thus, although using Hypre-BoomerAMG preconditioner can drastically reduce the number of solver iterations, it is not interesting (in terms of total computation time) to combine it with the HyprePCG solver for our case studies. The use of a HypreILU-type preconditioner reduces the number of solver iterations by a factor of 2 to 3 compared to the case without preconditioner, and also appears to be powerful in terms of computation time reduction. Consequently, its combination with HyprePCG solver is efficient and should be preferred for our contact problems.

A loss of performance is also observed in Figure 23 between 16 and 32 CPU cores. A conceivable explanation is that the intra-node bandwidth seen by the CPU core is higher for 16 cores than for 32.

For AMR Combination 2, similar scalability analyses were performed and are reported in Figure 24. The threshold values  $e_{\Omega,LOC} = 4\%$  and  $\delta = 0.1\%$ have been set to highlight the specificity of this combination of criteria for the same number of refinement steps as previously for AMR Combination 1. The observations and conclusions regarding the global scalability are the same as for the previous choice of AMR criteria. However, the MFEM function forming the linear system performs better than ideally for 128, 256 and 512 CPU cores, which is certainly due to the presence of cache effects as we use much more cache memory with an increasing number of nodes. Indeed, if an increasing number of cores are used, then it is typically possible to employ more and more fast caches simultaneously. In our case, on the topaze supercomputer, the L2 cache is 512 KB per core. Thus, this means there is more room for data to fit in the L2 cache for an increasing number of cores. In a strong scaling case, the total amount of data that can fit in the L2 cache increases with the number of cores. The superlinear speedups reported can be explained by these cache effects. More specifically, the hypre library routine hypre\_BoomerAMGBuildCoarseOperator is responsible for this superlinearity, and consists in performing the matrix operation defined by Equation (26). In addition, let us underline that, as the final number of conforming DOFs is almost half that for the previous AMR Combination 1 simulation, the total times are reduced accordingly.

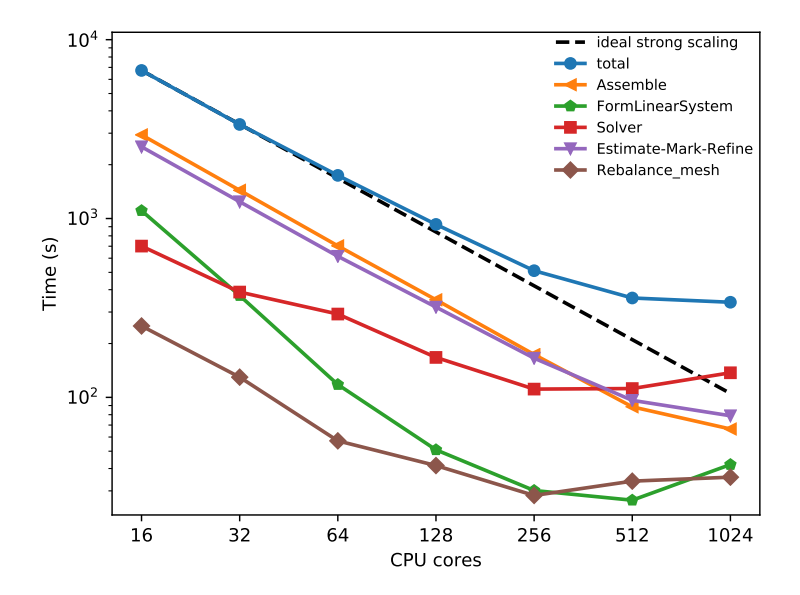


Figure 24: Performance results of the contact-AMR-HPC algorithm and its main steps - 3D Hertzian contact - AMR Combination 2 ( $e_{\Omega,LOC} = 4\%$ ,  $\delta = 0,1\%$ ) - HyprePCG solver with HypreILU preconditioner - number of final mesh conforming DOFs:  $5.1 \times 10^6$ .

#### 6. Conclusions

In this paper, a scalable non-conforming AMR strategy dedicated to elastostatic contact mechanics problems has been introduced. It has been developed in the MFEM library. It is based on the implementation of a node-to-node pairing combined with a penalization technique for contact solution. An efficient partitioning that gathers paired contact nodes together in the same parallel region is proposed. The MFEM parallelized algorithm for non-conforming h-refinement has been enriched by our own ESTIMATE-MARK-REFINE strategy. This strategy is in particular designed to be effective for contact problems with curved boundaries and quadrilateral/hexahedral first-order finite elements thanks to the use of super-parametric finite elements. Representative academic 2D and 3D examples confirm the accuracy of the proposed approach.

The proposed strategy makes it possible to combine both efficient parallelization and AMR techniques to solution 3D contact problems. This is an important novelty as the combination of these advanced numerical strategies was not previously considered. The robust strategy we propose is scalable across hundreds of processes and enables the treatment of problems with tens

of millions of unknowns. Ongoing studies will focus on the extension to contact treatment of classical geometric partitioning algorithms (Space-Filling Curve) and graph partitioning algorithms (using Metis software package [97]). A enhanced gain in scalability is expected with these partitionings.

Our strategy is aimed to be extended to more generic 3D contact mechanics solutions, enabling a wider range of problems to be considered. For example, an ongoing work is to implement node-to-surface pairing. The main issue relies on the definition of a relevant mesh partitioning. To solve industrial problems of interest, our strategy has also to be extended to non-linear mechanics. The MFEM-MGIS project [98, 99] may be used to this end, since the current standalone MFEM library only deals with elastic or hyperelastic mechanical behaviors. Finally time-dependent problems have to be considered, with a special attention to field transfer (for discretization error control) and load balancing (for computational time) issues between time steps.

# Acknowledgements

This work was developed within the framework of the MISTRAL joint research laboratory between Aix-Marseille University, CNRS, Centrale Marseille, and CEA (Commissariat à l'Énergie Atomique et aux Énergies Alternatives). The authors would like to acknowledge the High Performance Computing Center of CCRT for supporting this work by providing scientific support and access to computing resources. We also acknowledge financial support from the PICI2 project (CEA).

#### References

- [1] P. G. Ciarlet, The finite element method for elliptic problems, North-Holland, Amsterdam, New York, Oxford, 1978.
- [2] P. Wriggers, Computational contact mechanics. Second edition, Springer-Verlag, 2006.
- [3] L. B. da Veiga, F. Brezzi, L. Marini, Virtual elements for linear elasticity problems, SIAM J. Numer. Anal. 51 (2013).
- [4] P. Wriggers, F. Aldakheel, B. Hudobivnik, Virtual Element Methods in Engineering Sciences, Springer, 2023.

- [5] P. Wriggers, W. Rust, B. Reddy, A virtual element method for contact, Comput. Mech. 58 (2016).
- [6] M. Laaziri, R. Masson, VEM-Nitsche fully discrete polytopal scheme for frictionless contact-mechanics, SIAM J. Numer. Anal. 63 (1) (2025) 81–102. doi:10.1137/24M1660218.
- [7] D. A. Di Pietro, A. Ern, A hybrid high-order locking-free method for linear elasticity on general meshes, Comput. Methods Appl. Mech. Eng. 283 (2015) 1–21. doi:10.1016/j.cma.2014.09.009.
- [8] D. A. Di Pietro, J. Droniou, The hybrid high-order method for polytopal meshes. Design, analysis, and applications, Vol. 19 of MS&A, Model. Simul. Appl., Cham: Springer, 2020. doi:10.1007/ 978-3-030-37203-3.
- [9] F. Chouly, A. Ern, N. Pignet, A hybrid high-order discretization combined with Nitsche's method for contact and Tresca friction in small strain elasticity, SIAM J. Sci. Comput. 42 (4) (2020) a2300–a2324. doi:10.1137/19M1286499.
- [10] C. Song, J. P. Wolf, The scaled boundary finite-element method—alias consistent infinitesimal finite-element cell method—for elastodynamics, Computer Methods in Applied Mechanics and Engineering 147 (3) (1997) 329–355. doi:10.1016/S0045-7825(97)00021-2.
- [11] H. Hirshikesh, A. L. N. Pramod, E. T. Ooi, C. Song, S. Natarajan, An adaptive scaled boundary finite element method for contact analysis, Eur. J. Mech. A. Solids 86 (104180) (2021).
- [12] L. De Lorenzis, P. Wriggers, T. J. Hughes, Isogeometric contact: a review, GAMM-Mitteilungen 37 (1) (2014) 85-123. arXiv:https: //onlinelibrary.wiley.com/doi/pdf/10.1002/gamm.201410005, doi:https://doi.org/10.1002/gamm.201410005. URL https://onlinelibrary.wiley.com/doi/abs/10.1002/gamm. 201410005
- [13] J. A. Cottrell, T. J. Hughes, Y. Bazilevs, Isogeometric analysis: toward integration of CAD and FEA, John Wiley & Sons, 2009.

- [14] N. Kikuchi, J. T. Oden, Contact problems in elasticity: a study of variational inequalities and finite element methods, Vol. 8, SIAM Studies in Applied Mathematics, Society for Industrial and Applied Mathematics (SIAM), Philadelphia, PA, 1988.
- [15] T. A. Laursen, Computational contact and impact mechanics, Springer-Verlag, Berlin, 2002.
- [16] N. Kikuchi, Y. Song, Penalty/finite-element approximations of a class of unilateral problems in linear elasticity, Quart. Appl. Math. 39 (1) (1981) 1–22.
- [17] J. C. Simo, T. A. Laursen, An augmented Lagrangian treatment of contact problems involving friction, Comput. Struct. 42 (1992) 97–116.
- [18] P. Wriggers, G. Zavarise, A formulation for frictionless contact problems using a weak form introduced by nitsche, Comput. Mech. 41 (2008) 407–420.
- [19] F. Chouly, P. Hild, A nitsche-based method for unilateral contact problems: numerical analysis, SIAM J. Numer. Anal. 51 (2) (2013) 1295–1307.
- [20] F. B. Belgacem, P. Hild, P. Laborde, The mortar finite element method for contact problems, Mathematical and Computer Modeling 28 (1998) 263–271.
- [21] R. Verfürth, A review of a posteriori error estimation and adaptive meshrefinement techniques, Advances in Numerical Mathematics (1996).
- [22] L. Demkowicz, P. Devloo, J. Oden, On an h-type mesh-refinement strategy based on minimization of interpolation errors, Computer Methods in Applied Mechanics and Engineering 53 (1985) 67–89.
- [23] P. Dìez, A. Huerta, A unified approach to remeshing strategies for finite element h-adaptivity, Computer Methods in Applied Mechanics and Engineering 176 (1999) 215–229.
- [24] I. Babuška, B. Szabo, On the rates of convergence of the finite element method, International Journal for Numerical Methods in Engineering 18 (3) (1982) 323–341.

- [25] I. Babuška, B. Guo, The h, p and h-p version of the finite element method; basis theory and applications, Advances in Engineering Software 15 (3) (1992) 159–174.
- [26] O. Zienkiewicz, J. Zhu, N. Gong, Effective and practical h-p-version adaptive analysis procedures for the finite element method, International Journal for Numerical Methods in Engineering 28 (4) (1989) 879–891.
- [27] A. Brandt, Multi-level adaptive solutions to boundary-value problems, Mathematics of Computation 31 (1977) 333–390.
- [28] D. Bai, A. Brandt, Local mesh refinement multilevel techniques, SIAM Journal on Scientific and Statistical Computing 8 (1987) 109–134.
- [29] K. Khadra, P. Angot, J. P. Caltagirone, P. Morel, Concept de zoom adaptatif en architecture multigrille locale; étude comparative des méthodes l.d.c., f.a.c. et f.i.c., ESAIM: Mathematical Modelling and Numerical Analysis Modélisation Mathématique et Analyse Numérique 30 (1) (1996) 39–82.
- [30] O. C. Zienkiewicz, J. Z. Zhu, A simple error estimator and adaptive procedure for practical engineering analysis, International Journal for Numerical Methods in Engineering 24 (1987) 337–357.
- [31] H. Liu, I. Ramière, F. Lebon, On the coupling of local multilevel mesh refinement and ZZ methods for unilateral frictional contact problems in elastostatics, Computer Methods in Applied Mechanics and Engineering 323 (2017) 1–26.
- [32] P. Wriggers, O. Scherf, Different a posteriori error estimators and indicators for contact problems, Mathematical and Computer Modelling 28 (4-8) (1998) 437–447.
- [33] D. Braess, C. Carstensen, R. Hoppe, Convergence analysis of a conforming adaptive finite element method for an obstacle problem, Numerische Mathematik 107 (3) (2007) 455–471. doi:10.1007/s00211-007-0098-6.
- [34] T. Gustafsson, R. Stenberg, J. Videman, On nitsche's method for elastic contact problems, SIAM Journal on Scientific Computing 42 (2) (2020) B425–B446. doi:10.1137/19M1246869.

- [35] R. Araya, F. Chouly, Residual a posteriori error estimation for frictional contact with nitsche method, Journal of Scientific Computing 96 (87) (08 2023). doi:10.1007/s10915-023-02300-8.
- [36] V. Roda-Casanova, F. Sanchez-Marin, An adaptive mesh refinement approach for solving non-hertzian elastic contact problems, Meccanica 53 (2018) 2013–2028. doi:10.1007/s11012-017-0806-y.
- [37] A. Rademacher, Mesh and model adaptivity for frictional contact problems, Numerische Mathematik 142 (3) (2019) 465–523. doi:10.1007/s00211-019-01044-8.
- [38] H. Boffy, M.-C. Baietto, P. Sainsot, T. Lubrecht, An efficient 3d model of heterogeneous materials for elastic contact applications using multigrid methods, Journal of Tribology-Transactions of the Asme 134 (2) (2012) 021401. doi:10.1115/1.4006296.
- [39] C. Song, E. T. Ooi, A. L. N. Pramod, S. Natarajan, A novel error indicator and an adaptive refinement technique using the scaled boundary finite element method, Engineering Analysis with Boundary Elements 94 (2018) 10-24. doi:https://doi.org/10.1016/j.enganabound.2018.05.010.

  URL https://www.sciencedirect.com/science/article/pii/S0955799718300407
- [40] F. Aldakheel, B. Hudobivnik, E. Artioli, L. Beirão da Veiga, P. Wriggers, Curvilinear virtual elements for contact mechanics, Computer Methods in Applied Mechanics and Engineering 372 (2020) 113394. doi:https://doi.org/10.1016/j.cma.2020.113394.
- [41] M. Cihan, B. Hudobivnik, J. Korelc, P. Wriggers, A virtual element method for 3d contact problems with non-conforming meshes, Comput. Methods Appl. Mech. Engrg. 402 (115385) (2022). URL https://doi.org/10.1016/j.cma.2022.115385
- [42] J. Flaherty, R. Loy, M. Shephard, B. Szymanski, J. Teresco, L. Ziantz, Adaptive local refinement with octree load balancing for the parallel solution of three-dimensional conservation laws, J. Parallel Distrib. Comput. 47 (1997) 139–152.

- [43] T. Tu, D. O'Hallaron, O. Ghattas, Scalable parallel octree meshing for terascale applications, in: Proceedings of the 2005 ACM/IEEE Conference on Supercomputing, IEEE Computer Society, 2005.
- [44] W. F. Mitchell, A refinement-tree based partitioning method for dynamic load balancing with adaptively refined grids, J. Parallel Distrib. Comput. 67 (2007) 417–429.
- [45] H. Sundar, R. Sampath, G. Biros, Bottom-up construction and 2:1 balance refinement of linear octrees in parallel, SIAM Journal on Scientific Computing 30 (2008) 2675–2708.
- [46] C. Burstedde, L. C. Wilcox, O. Ghattas, p4est: Scalable algorithms for parallel adaptive mesh refinement on forests of octrees, SIAM Journal on Scientific Computing 33 (2011) 1103–1133.
- [47] C. Burstedde, Parallel tree algorithms for amr and non-standard data access, ACM Transactions on Mathematical Software 46 (2020) 1–31.
- [48] P. Munch, K. Ljungkvist, M. Kronbichler, Efficient application of hanging-node constraints for matrix-free high-order FEM computations on CPU and GPU, in: Proceedings of the High performance computing: 37th international conference, ISC High Performance, Lecture Notes in Computer Science, Vol. 13289, Springer, 2022.
- [49] D. Arndt, W. Bangerth, D. Davydov, T. Heister, L. Heltai, M. Kronbichler, M. Maier, J.-P. Pelteret, B. Turcksin, D. Wells, The deal.II finite element library: Design, features, and insights, Computers & Mathematics with Applications 81 (2021) 407-422, development and Application of Open-source Software for Problems with Numerical PDEs. doi:10.1016/j.camwa.2020.02.022.
  URL https://www.sciencedirect.com/science/article/pii/S0898122120300894
- [50] R. Anderson, J. Andrej, A. Barker, J. Bramwell, J.-S. Camier, J. Červený, V. Dobrev, Y. Dudouit, A. Fisher, T. Kolev, W. Pazner, M. Stowell, V. Tomov, J. Dahm, D. Medina, S. Zampini, MFEM: a modular finite element methods library, Computers & Mathematics with
  - URL https://doi.org/10.1016/j.camwa.2020.06.009

Applications (2020).

- [51] L. Kaczmarczyk, Z. Ullah, K. Lewandowski, X. Meng, X.-Y. Zhou, I. Athanasiadis, H. Nguyen, C.-A. Chalons-Mouriesse, E. J. Richardson, E. Miur, A. G. Shvarts, M. Wakeni, C. J. Pearce, Mofem: An open source, parallel finite element library, Journal of Open Source Software 5 (2020) 1441/1–8.
- [52] M. S. Alnæs, J. Blechta, J. Hake, A. Johansson, B. Kehlet, A. Logg, C. Richardson, J. Ring, M. E. Rognes, G. N. Wells, The fenics project version 1.5, Archive of Numerical Software 3 (2015) 9–23.
- [53] F. Hecht, New development in freefem++, J. Numer. Math. 20 (2012) 251–265.
- [54] B. S. Kirk, J. W. Peterson, R. H. Stogner, G. F. Carey, library for parallel adaptive mesh refinement/coarsening simulations, Engineering with Computers 22 (2006) 237–254.
- [55] M. Barboteu, P. Alart, M. Vidrascu, A domain decomposition strategy for non-classical frictional multi-contact problems, Comp. Meth. Appl. Mech. Engrg 190 (2001) 4785–4803.
- [56] D. Dureisseix, C. Farhat, A numerically scalable domain decomposition method for the solution of frictionless contact problems, Int. J. Num. Meth. Engrg 50 (2001) 2643–2666.
- [57] P. Alart, Contact on Multiprocessor Environment: from Multicontact Problems to Multiscale Approaches, Computational Contact Mechanics, Springer, Vienna, 2007.
- [58] J. Har, R. E. Fulton, A parallel finite element procedure for contact-impact problems, Engineering with Computers 19 (2003) 67–84.
- [59] T. A. Wiesner, M. Mayr, A. Popp, M. W. Gee, W. A. Wall, Algebraic multigrid methods for saddle point systems arising from mortar contact formulations, International Journal for Numerical Methods in Engineering 122 (15) (2021) 3749–3779. doi:10.1002/nme.6680.
- [60] A. Franceschini, M. Ferronato, M. Frigo, C. Janna, A reverse augmented constraint preconditioner for Lagrange multiplier methods in contact mechanics, Comput. Methods Appl. Mech. Eng. 392 (2022).

- [61] G. Guillamet, M. Rivero, M. Zavala-Aké, M. Vázquez, G. Houzeaux, S. Oller, A parallel algorithm for unilateral contact problems, Computers & Structures 271 (2022).
- [62] Z. Dostál, T. Kozubek, M. Sadowská, V. Vondrák, Scalable algorithms for contact problems, Springer, 2023.
- [63] M. Mayr, A. Popp, Scalable computational kernels for mortar finite element methods, Engineering with Computers 39 (2023) 3691–3720.
- [64] J. Frohne, T. Heister, W. Bangerth, Efficient numerical methods for the large-scale, parallel solution of elastoplastic contact problems, Int. J. Numer. Methods Eng. 105 (2016) 416–439.
- [65] D. W. Kelly, J. P. De S. R. Gago, O. C. Zienkiewicz, I. Babuska, A posteriori error analysis and adaptive processes in the finite element method: Part i—error analysis, International Journal for Numerical Methods in Engineering 19 (11) (1983) 1593–1619. doi:10.1002/nme.1620191103.
- [66] T. Belytschko, C. Parimi, N. Moës, N. Sukumar, S. Usui, Structured extended finite element methods for solids defined by implicit surfaces, International Journal for Numerical Methods in Engineering 56 (2003) 609–635.
- [67] I. Ramière, P. Angot, M. Belliard, A fictitious domain approach with spread interface for elliptic problems with general boundary conditions, Computer Methods in Applied Mechanics and Engineering 196 (2007) 766-781.
- [68] B. Michel, C. Nonon, J. Sercombe, F. Michel, V. Marelle, Simulation of pellet-cladding interaction with the pleiades fuel performance software environment, Nuclear Technology 182 (2013) 124–137.
- [69] J. Z. Zhu, E. Hinton, O. C. Zienkiewicz, Mesh enrichment against mesh regeneration using quadrilateral elements, Communications in Numerical Methods in Engineering 9 (1993) 547–554.
- [70] J. Ródenas, J. Albelda, M. Tur, F. Fuenmayor, A hierarchical h-adaptivity methodology based on element subdivision, Revista UIS Ingenierías 16 (2017) 263–280.

- [71] I. Babuška, A. Miller, M. Vogelius, Adaptive methods and error estimation for elliptic problems of structural mechanics, Adaptive Computational Methods for Partial Differential Equations (1983) 57–73.
- [72] P. Hennig, M. Kastner, P. Morgenstern, D. Peterseim, Adaptive mesh refinement strategies in isogeometric analysis - a computational comparison, Computer Methods in Applied Mechanics and Engineering 316 (2016) 424–448.
- [73] D. Koliesnikova, I. Ramière, F. Lebon, A unified framework for the computational comparison of adaptive mesh refinement strategies for all-quadrilateral and all-hexahedral meshes: Locally adaptive multigrid methods versus h-adaptive methods, Journal of Computational Physics 437 (2021).
- [74] J. Červený, V. Dobrev, T. Kolev, Non-conforming mesh refinement for high-order finite elements, SIAM J. Sci. Comput. 41 (4) (2019) C367— C392.
   URL http://dx.doi.org/10.1137/18M1193992
- [75] P. E. Farrell, S. Micheletti, S. Perotto, An anisotropic zienkiewicz-zhutype error estimator for 3D applications, International Journal for Numerical Methods in Engineering 85 (6) (2011) 671-692. doi:10.1002/nme.2980.
- [76] F. Nataf, P.-H. Tournier, A GenEO Domain Decomposition method for Saddle Point problems, Comptes Rendus. Mécanique 351 (S1) (2023) 667–684. doi:10.5802/crmeca.175.
- [77] D. G. Luenberger, Linear and Nonlinear Programming, Addison-Wesley, Reading, Mass., second edition, 1984.
- [78] S. Jin, D. Sohn, S. Im, Node-to-node scheme for three-dimensional contact mechanics using polyhedral type variable-node elements, Computer Methods in Applied Mechanics and Engineering 304 (2016) 217-242. doi:https://doi.org/10.1016/j.cma.2016.02.019.
  URL https://www.sciencedirect.com/science/article/pii/S0045782516300494
- [79] W. Xing, J. Zhang, C. Song, F. Tin-Loi, A node-to-node scheme for three-dimensional contact problems using the

- scaled boundary finite element method, Computer Methods Applied Mechanics and Engineering 347(2019)928-956. doi:https://doi.org/10.1016/j.cma.2019.01.015. URL https://www.sciencedirect.com/science/article/pii/ S0045782519300209
- [80] J. J. Moreau, On unilateral constraints, friction and plasticity, G. Capriz and G. Stampacchia, editors, New Variational Techniques in Mathematical Physics, CIME, Roma, 1974.
- [81] A. Curnier, Unilateral contact: Mechanical modelling, P. Wriggers and P. Panagiotopoulos, editors, New Developments in Contact Problems, Springer, Wien, 1999.
- [82] R. H. Nochetto, A. Veeser, Primer of Adaptive Finite Element Methods, Springer Berlin Heidelberg, 2012.
- [83] W. Dörfler, A convergent adaptive algorithm for poisson's equation, SIAM Journal on Numerical Analysis 33 (1996) 1106–1124.
- [84] L. Barbié, I. Ramière, F. Lebon, An automatic multilevel refinement technique based on nested local meshes for nonlinear mechanics, Computers and Structures 147 (2015) 14–25.
- [85] I. Ramière, H. Liu, F. Lebon, Original geometrical stopping criteria associated to multilevel adaptive mesh refinement for problems with local singularities, Computational Mechanics (2019).
- [86] J. R. Pilkington, S. B. Baden, Partitioning with spacefilling curves, Tech. rep., Department of Computer Science and Engineering, University of California, San Diego (1994).
- [87] S. Aluru, F. Sevilgen, Parallel domain decomposition and load balancing using space-filling curves, in: Proceedings Fourth International Conference on High-Performance Computing, IEEE Comput. Soc., 1997, pp. 230–235. doi:10.1109/HIPC.1997.634498.
- [88] C. Geuzaine, J.-F. Remacle, Gmsh: a three-dimensional finite element mesh generator with built-in pre- and post-processing facilities, International Journal for Numerical Methods in Engineering 79 (11) (2009) 1309–1331.

- [89] H. Hertz, On the Contact of Rigid Elastic Solids and on Hardness, Macmillan and Co., New York, 1882. URL https://archive.org/details/cu31924012500306
- [90] G. Zavarise, The shifted penalty method, Comput. Mech. 56 (2015) 1–17.
- [91] F. Chouly, P. Hild, On convergence of the penalty method for unilateral contact problems, Applied Numerical Mathematics 65 (2013) 27–40.
- [92] CEA, Cast3m (2023). URL https://www.cast3m.cea.fr
- [93] G. Drouet, P. Hild, Optimal convergence for discrete variational inequalities modelling signorini contact in 2d and 3d without additional assumptions on the unknown contact set, SIAM Journal on Numerical Analysis 53 (3) (2015) 1488–1507. doi:10.1137/140980697. URL https://doi.org/10.1137/140980697
- [94] B. Wohlmuth, A. Popp, M. Gee, W. Wall, An abstract framework for a priori estimates for contact problems in 3d with quadratic finite elements, Computational Mechanics 49 (6) (06 2012). doi:10.1007/ s00466-012-0704-z.
- [95] D. Böhme, F. Wolf, B. R. de Supinski, M. Schulz, M. Geimer, Scalable critical-path based performance analysis, in: 26th International Parallel and Distributed Processing Symposium, IEEE, 2012, pp. 1330–1340. doi:10.1109/IPDPS.2012.120.
- [96] INL, Moose (2023).
   URL https://mooseframework.inl.gov/application\_usage/
   hypre.html
- [97] G. Karypis, V. Kumar, Metis: A software package for partitioning unstructured graphs, partitioning meshes, and computing fill-reducing orderings of sparse matrices, Tech. rep., University of Minnesota, Department of Computer Science / Army HPC Research Center Minneapolis, MN 55455 (1998).

- [98] T. Helfer, G. Latu, R. Prat, M. Wangermez, F. Cuteri, MFEM/MGIS, a HPC mini-application targeting nonlinear thermo-mechanical simulations of nuclear fuels at mesoscale, Journal of Open Source Software 10 (108) (2025) 7719. doi:10.21105/joss.07719. URL https://doi.org/10.21105/joss.07719
- [99] T. Helfer, The MFEM/MGIS project. URL https://thelfer.github.io/mfem-mgis/